ELSEVIER

NeuroImage

www.elsevier.com/locate/ynimg
NeuroImage xx (2004) xxx–xxx

Brain structural mapping using a novel hybrid implicit/explicit framework based on the level-set method

A. Leow,[a,*] C.L. Yu,[b] S.J. Lee,[c] S.C. Huang,[d] H. Protas,[d] R. Nicolson,[e] K.M. Hayashi,[a] A.W. Toga,[a] and P.M. Thompson[a]

[a]*Department of Neurology, Laboratory of Neuro Imaging, UCLA School of Medicine, Los Angeles, CA 90095, USA*
[b]*Department of Molecular and Medical Pharmacology at UCLA School of Medicine, Los Angeles, CA 90095, USA*
[c]*Department of Electronic Engineering, Paichai University, Daejeon, South Korea*
[d]*Department of Biomathematics and the Department of Molecular and Medical Pharmacology at UCLA School of Medicine, Los Angeles, CA 90095, USA*
[e]*Department of Psychiatry, University of Western Ontario, London, ON, Canada*

Received 29 July 2004; revised 8 September 2004; accepted 15 September 2004

This paper presents a novel approach to feature-based brain image warping, by using a hybrid implicit/explicit framework, which unifies many prior approaches in a common framework. In the first step, we develop links between image warping and the level-set method, and we formulate the fundamental mathematics required for this hybrid implicit/explicit approach. In the second step, we incorporate the large-deformation models into these formulations, leading to a complete and elegant treatment of anatomical structure matching. In this latest approach, exact matching of anatomy is achieved by comparing the target to the warped source structure under the forward mapping and the source to the warped target structure under the backward mapping. Because anatomy is represented nonparametrically, a path is constructed linking the source to the target structure without prior knowledge of their point correspondence. The final point correspondence is constructed based on the linking path with the minimal energy. Intensity-similarity measures can be naturally incorporated in the same framework as landmark constraints by combining them in the gradient descent body forces. We illustrate the approach with two applications: (1) tensor-based morphometry of the corpus callosum in autistic children; and (2) matching cortical surfaces to measure the profile of cortical anatomic variation. In summary, the new mathematical techniques introduced here contribute fundamentally to the mapping of brain structure and its variation and provide a framework that unites feature and intensity-based image registration techniques.

Keywords: Structural mapping; Implicit/explicit framework; Level-set method

Introduction

Nonlinear image registration is a key step in the analysis of brain imaging data, with broad applications in brain mapping and computational anatomy. Registration techniques are commonly used to nonlinearly deform functional or structural images from individual subjects to match the shape of a neuroanatomic atlas, or a group average image template (Ashburner et al., 1998; Collins et al., 1995; Woods et al., 1998; Zeineh et al., 2003). This step reduces subject-specific anatomic shape differences, making it easier to compare PET or functional MRI data across subjects, and sensitizing the detection of experimental effects. In a related application, maps that visualize patterns of structural brain change over time can be created by nonlinearly warping a baseline MRI scan to match a subsequent scan from the same subject (Janke et al., 2001; Rey et al., 1999; Thompson et al., 2000a,b). Brain regions undergoing rapid growth or atrophy can be identified, and the resulting maps can be analyzed using tensor-based morphometry techniques (Chung et al., 2001; Shen and Davatzikos, 2003; Studholme et al., 2004; Thirion et al., 2000). Finally, brain image warping techniques play a key role in computational anatomy (Lancaster et al., 2003; Miller, 2004; Toga, 1998). Deformation fields, from nonlinear warping algorithms, allow computation of average shape models and average brain templates. They also

* Corresponding author. Department of Neurology, Laboratory of Neuro Imaging, UCLA School of Medicine, Room 4238, 710 Westwood Plaza, Los Angeles, CA 90095. Fax: +1 310 206 5518.
E-mail addresses: feuillet@ucla.edu (A. Leow), clyu@ucla.edu (C.L. Yu), sjlee@pcu.ac.kr (S.J. Lee), hhuang@mednet.ucla.edu (S.C. Huang), hprotas@ucla.edu (H. Protas), rnicolso@uwo.ca (R. Nicolson), khayashi@loni.ucla.edu (K.M. Hayashi), toga@loni.ucla.edu (A.W. Toga), thompson@loni.ucla.edu (P.M. Thompson).
Available online on ScienceDirect (www.sciencedirect.com.)

1053-8119/$ - see front matter © 2004 Elsevier Inc. All rights reserved.
doi:10.1016/j.neuroimage.2004.09.022

generate asymmetry and variability measures for brain structures, and enable disease and developmental processes to be tracked and visualized (Gogtay et al., 2004; Thompson et al., 2004).

The information typically used for brain warping includes image intensity (Bajcsy and Kovacic, 1989; Christensen et al., 1996; Woods et al., 1993, 1998), or landmarks in the form of points (Bookstein, 1978; Joshi and Miller, 2000; Rohr et al., 1996), curves (Davatzikos et al., 1996b; Subsol, 1999), and surfaces (Thompson and Toga, 1996). Recently, different types of information such as intensity and convexity/concavity profile have been combined in the registration process, especially in applications such as cortical surface registration (Fischl et al., 1999, 2001). However, it is also known that intensity-similarity cost functionals are relatively difficult to combine with landmark constraints that can significantly improve the accuracy and stability of image registration.

In computational anatomy, it can also be advantageous for image registration to be carried out in a diffeomorphic way (Christensen et al., 1996; Miller, 2004). In this case, the transformation defining the correspondence map should be a one-to-one, onto, and differentiable map from the image domain back onto itself, while aligning the important structures. To make the transformation smooth, regularization (i.e., spatial smoothing) of the displacement vector field is often necessary. Regularization techniques have emerged from related work in diverse fields such as Gaussian smoothing, scale-space theory, and inverse problems (Nielsen et al., 1994; Tikhonov and Arsenin, 1977), thin-plate spline warping or kriging (Bookstein, 1978), elastic operator warping (Bajcsy and Kovacic, 1989; Joshi et al., 1995), large deformation fluid dynamic matching (Bro-Nielsen and Gramkow, 1996; Christensen et al., 1996, 1997), and large deformation diffeomorphic metric mapping (Miller, 2004). Many groups have been actively developing regularization techniques for brain image matching, but less effort has been devoted to examining the matching cost functionals systematically.

In this paper, we propose a novel theory of feature-based image matching using a hybrid explicit/implicit framework. Our group is among the first to introduce implicit representations and the level-set method (Osher and Sethian, 1988) into image warping using a Lagrangian reference frame. This paper builds on our previous work of nonlinear feature warping with implicit representations (Leow et al., 2004a,b; Liao, 2003; Liao et al., 2003). In our previous approach, the proposed techniques for both linear and nonlinear matching were closely related to the minimization of the Hausdorff metric between geometric features due to the implicit formulations. Moreover, we were able to reformulate cost functionals for matching geometric features of different natures (e.g., point constraints in the case of point matching, line integral constraints in the case of curve matching, and surface integral constraints in the case of surface matching) into similar variational forms involving integrals on the whole image domain. However, our previous approach was limited in its practical use by the difficulty in automatically generating the implicit representations for curves or surfaces. This paper extends our previous work and introduces a modified framework in which no explicit computation of the level-set functions is needed anymore. That is why we used the term hybrid implicit/explicit in the title. Moreover, the proposed matching cost functional now works for all types of geometric features regardless of their nature (in previous approaches, different types of features required different types of matching cost functions).

The level-set method we used in this paper is in a modified Lagrangian framework and thus the formulations are inherently different from the traditional level-set method. In our case, the level-set functions are updated in a Lagrangian reference frame by solving for the displacement field and propagating the level-set functions based upon the displacement field instead of the original Eulerian reference frame (i.e., updating the level-set functions on the grid points). It is true that some of the well-known advantages of the level-set method (e.g., easily handling changes in object topology) are not really utilized in this paper. However, because of this Lagrangian nature, we show that the nonlinear image registration framework can be linked to the techniques/formulations in the level-set method elegantly. Specifically, our formulation allows cost functionals to be transformed into a common integral form. Standard techniques such as Euler–Lagrange equations and the gradient descent method can then be applied. We believe that this is the first attempt in this direction where the concept of implicit representations and image warping are brought together with a rigorous foundation.

Most feature-based registration techniques depend on first establishing an explicit point correspondence between features such that point matching techniques can be applied. Instead, our new approach treats these features as a whole, so no prior knowledge is required regarding the internal point correspondences between two features. This allows sliding when registering geometric features and has significant theoretical and practical impact, allowing maps with less geometric distortion.

Overview of paper

We devote the first part of the paper to a detailed discussion of this novel feature mapping technique. In the second part of the paper, the approach is rigorously combined with a large deformation model that leads to a complete treatment of nonlinear brain image registration under both small and large deformation models. Large deformation models are increasingly advocated in computational anatomy (e.g., by Avants and Gee, 2004; Christensen et al., 1996; Grenander and Miller, 1998; Joshi et al., 1995; Miller, 2004) as they can accommodate arbitrarily large anatomic differences while prohibiting tearing or folding of the deforming image. Finally, we report the results of applying these techniques to two brain mapping problems: modeling cortical anatomic variability in 3D and mapping anatomic shape differences of the corpus callosum in autism.

Theory and methods

The task of image registration is finding a one-to-one transformation h that maps a source image $S(x)$ defined in the image domain Ω to a target image $T(x)$. Traditionally, the transformation h is expressed in terms of its displacement field u: $h(x) = x - u(x)$. The inverse map h^{-1} of h maps the target back to the source image with the notation u^{-1} denoting the displacement field of h^{-1}. In this paper, a point x in 2D is represented by $x = (x_1, x_2)$ with u_1 and u_2 denoting the x_1 and x_2 components of u (similarly, u_1^{-1} and u_2^{-1} the components of u^{-1}). Similar notations will also be used in 3D.

Moving points in 2D and 3D

We now examine geometric feature constraints that include points, open curves and surfaces in 2D and 3D. The fundamental formulation upon which we will build our matching strategy is moving a point P along the gradient of a scalar function. We first describe how to extract a point value of a function through an integral defined on the whole domain using implicit representations. In 2D, suppose we have a continuous scalar-valued function $G(x)$ defined in the whole image domain Ω and level-set functions ϕ_1 and ϕ_2 such that the intersection of their zero level sets is the point $P = (p_1, p_2)$ inside Ω. Then, we have the following

$$\begin{aligned} G(P) &= \int G(x)\delta(\phi_1)\delta(\phi_2)|\nabla\phi_1||P_{\nabla\phi_1}\nabla\phi_2|\mathrm{d}x \\ &= \int G(x)\delta(\phi_1)\delta(\phi_2)|\nabla\phi_2||P_{\nabla\phi_2}\nabla\phi_1|\mathrm{d}x \\ &= \int G(x)\delta(\phi_1)\delta(\phi_2)|\nabla\phi_1 \times \nabla\phi_2|\mathrm{d}x. \end{aligned} \tag{1}$$

Here δ is the Dirac delta function and P_v is the projection operator of a vector v that projects another vector onto the direction orthogonal to v, i.e., $P_{v_1}v_2 = v_2 - (v_1 \cdot v_2 / |v_1|^2)v_1$.

The derivations for Eq. (1) are provided in Appendix A (also refer to Bertalmío et al., 1999; Burchard et al., 2001; Cheng et al., 2002 for different derivations and more discussions on using intersections of level sets to represent geometric concepts in settings different from this paper). An intuitive way to understand Eq. (1) is to recognize the scaling factor $|\nabla\phi_1 \times \nabla\phi_2|$ as the area of the parallelogram with edge vector $\nabla\phi_1$ and $\nabla\phi_2$.

With a transformation h acting on source image S represented by its displacement field u and its inverse field u^{-1}, let us define the following notations to simplify our derivation

$$\tilde{\phi}_1(x) = \phi_1 \circ h = \phi_1(x-u);\ \tilde{\phi}_2(x) = \phi_2 \circ h = \phi_2(x-u). \tag{2}$$

For any point P on S, the displaced position $\tilde{P} = (\tilde{p}_1, \tilde{p}_2)$ of P on the deformed image $S \circ h = S(h(x))$ is simply

$$\tilde{p}_1 = p_1 - u_1^{-1}(P);\ \tilde{p}_2 = p_2 - u_2^{-1}(P). \tag{3}$$

Thus, $\tilde{P}$ is the intersection of the zero level sets of $\tilde{\phi}_1$ and $\tilde{\phi}_2$ given P the intersection of the zero level sets of ϕ_1 and ϕ_2. We can also view $\tilde{P}$ as the position of P under the action of the inverse map h^{-1}, and thus the alternative notation $\tilde{P} = P|_{h^{-1}}$ will also be used. Thus, the problem of finding the minimum of $G(x)$ starting from the initial position P in an image registration framework (i.e., solving u such that $G(\tilde{P})$ is the minimum of G) can be recast as solving the following minimization problem:

$$\begin{aligned} \min_u G(\tilde{P}) &= \min_u \int G(x)\delta(\tilde{\phi}_1)\delta(\tilde{\phi}_2)|\nabla\tilde{\phi}_1 \times \nabla\tilde{\phi}_2|\mathrm{d}x \\ &= \min_u \int G(x)\delta(\phi_1(x-u))\delta(\phi_2(x-u))|\nabla(\phi_1(x-u)) \times \nabla(\phi_2(x-u))|\mathrm{d}x. \end{aligned} \tag{4}$$

As proved in Appendix B, the body force (i.e., the steepest descent direction) with respect to the displacement field u of the minimization problem in Eq. (4) is

$$-\mathrm{div}\left(\frac{P_{\nabla\tilde{\phi}_2}\nabla\tilde{\phi}_1}{|P_{\nabla\tilde{\phi}_2}\nabla\tilde{\phi}_1|}|\nabla\tilde{\phi}_2|G\right)\delta(\tilde{\phi}_1)\delta(\tilde{\phi}_2)\nabla\tilde{\phi}_1 - \mathrm{div}\left(\frac{P_{\nabla\tilde{\phi}_1}\nabla\tilde{\phi}_2}{|P_{\nabla\tilde{\phi}_1}\nabla\tilde{\phi}_2|}|\nabla\tilde{\phi}_2|G\right)\delta(\tilde{\phi}_1)\delta(\tilde{\phi}_2)\nabla\tilde{\phi}_2. \tag{5}$$

Notice that in Burchard et al. (2001), similar formulations to Eq. (5) were used for evolving curves under length-minimizing motion (i.e., curvature motion) in 3D, and the delta functions were replaced with quantities resulting in curve evolution with curvature speed along the normal direction. Furthermore, by eliminating delta functions, the corresponding evolution equation can be implemented in a simpler fashion without numerical approximations of the delta functions. In our case, however, the proposed body force in Eq. (5) is active only at the intersection of the two zero level sets and thus the use of delta functions is necessary.

To simplify derivations in later sections, we will use the following form to denote Eq. (5)

$$\prod_{n=1}^{2}\delta(\phi_n \circ h)\sum_{n=1}^{2} f_n(G, \Phi \circ h)\nabla(\phi_n \circ h). \tag{6}$$

Here the capital level-set function denotes the collection of all level-set functions.

$$\Phi = (\phi_1, \phi_2); \Phi \circ h = (\phi_1 \circ h, \phi_2 \circ h). \tag{7}$$

These basic formulations have their counterparts in 3D where we can extract the point value of a function $G(x)$ at a point P repreented by the intersection of the zero level sets of ϕ_1, ϕ_2, and ϕ_3

$$\begin{aligned}\int G(x)\delta(\phi_1)\delta(\phi_2)\delta(\phi_3)|\nabla\phi_1 \times \nabla\phi_2 \cdot \nabla\phi_3|\mathrm{d}x &= \int G(x)\delta(\phi_1)\delta(\phi_2)\delta(\phi_3)|\nabla\phi_3 \times \nabla\phi_2 \cdot \nabla\phi_1|\mathrm{d}x \\ &= \int G(x)\delta(\phi_1)\delta(\phi_2)\delta(\phi_3)|\nabla\phi_1 \times \nabla\phi_3 \cdot \nabla\phi_2|\mathrm{d}x \\ &= G(P).\end{aligned} \tag{8}$$

As in Eq. (4), the registration problem of moving P toward the minimum of G becomes

$$\min_u \int G(x)\delta(\tilde{\phi_1})\delta(\tilde{\phi_2})\delta(\tilde{\phi_3})|\nabla\tilde{\phi_1} \times \nabla\tilde{\phi_2} \cdot \nabla\tilde{\phi_3}|\mathrm{d}x = \min_u G(\tilde{P}). \tag{9}$$

Eq. (8) can be derived similarly as in Eq. (1) (please refer to Liao, 2003 for detailed derivations), and an intuitive way to understand this result is to recognize that the scaling factor $|\nabla\phi_1 \times \nabla\phi_2 \cdot \nabla\phi_3|$ as the volume of a parallelepiped with edge vector $\nabla\phi_1$, $\nabla\phi_2$, and $\nabla\phi_3$.

The body force of the proposed registration problem (Eq. (9)) with respect to the displacement u is

$$\begin{aligned}&-\mathrm{div}\left[G(x)\mathrm{sgn}\left(\nabla\tilde{\phi_2} \times \nabla\tilde{\phi_3} \cdot \nabla\tilde{\phi_1}\right)\nabla\tilde{\phi_2} \times \nabla\tilde{\phi_3}\right]\delta(\tilde{\phi_1})\delta(\tilde{\phi_2})\delta(\tilde{\phi_3})\nabla\tilde{\phi_1} - \mathrm{div}\left[G(x)\mathrm{sgn}\left(\nabla\tilde{\phi_3} \times \nabla\tilde{\phi_1} \cdot \nabla\tilde{\phi_2}\right)\nabla\tilde{\phi_3} \times \nabla\tilde{\phi_1}\right] \\ &\times \delta(\tilde{\phi_1})\delta(\tilde{\phi_2})\delta(\tilde{\phi_3})\nabla\tilde{\phi_2} - \mathrm{div}\left[G(x)\mathrm{sgn}\left(\nabla\tilde{\phi_1} \times \nabla\tilde{\phi_2} \cdot \nabla\tilde{\phi_3}\right)\nabla\tilde{\phi_1} \times \nabla\tilde{\phi_2}\right]\delta(\tilde{\phi_1})\delta(\tilde{\phi_2})\delta(\tilde{\phi_3})\nabla\tilde{\phi_3}.\end{aligned} \tag{10}$$

For simplicity, we omit the derivations of the above results and refer the readers to (Liao, 2003) for a complete discussion. Notice that the body force in the 3D case can be expressed in the same form as in Eq. (6), with n running from 1 to 3.

Geometric feature matching under small deformation models

In our previous work (Leow et al., 2004a,b; Liao, 2003; Liao et al., 2003), we investigated the matching of anatomic structures by directly constructing their implicit level-set representations. This approach has been used to register brain surfaces subject to sulcal constraints and promising results have been reported (Leow et al., 2004a). However, a big challenge in this approach is how to automatically construct the implicit functions representing anatomic structures. We now propose new strategies that no longer require computation of the implicit representations, by utilizing the formulations developed in "Moving points in 2D and 3D" section.

Assume we have two anatomic structures of the same type (2D curves/shapes, or 3D curves/surfaces/volumes) in the source and target that we wish to match, and let the object in the source image be represented by a collection of discretized points $\{P^i\}$ and T_P be the unsigned distance function to this discretized point set. Similarly, let the anatomic structure in the target image be represented by the point set $\{Q^j\}$ and unsigned distance function T_Q. In 2D, let the level-set functions ϕ_1^i, ϕ_2^i be constructed such that P^i is the intersection of their zero level sets and similarly define ψ_1^j, ψ_2^j with respect to Q^j (in the case of 3D, a third level-set function is needed). Recalling the results Eqs. (1) and (8), we minimize the following cost function for matching the two anatomic structures in the small deformation setting where the warping field is constructed through the calculation of its displacement field

$$\begin{aligned}&\min_u \left[\sum_i T_Q(\tilde{P}^i) + \sum_j \tilde{T}_P(Q^j)\right] \\ &= \left\{\begin{array}{l} \min_u \left\{\begin{array}{l} \sum_i \int T_Q\delta\left(\tilde{\phi_1^i}\right)\delta\left(\tilde{\phi_2^i}\right)|\nabla\tilde{\phi}_1^i \times \nabla\tilde{\phi}_2^i|\mathrm{d}x \\ + \sum_j \int \tilde{T}_P\delta(\psi_1^j)\delta(\psi_2^j)|\nabla\psi_1^j \times \nabla\psi_2^j|\mathrm{d}x \end{array}\right\} \text{in 2D} \\ \min_u \left\{\begin{array}{l} \sum_i \left(\int T_Q\delta\left(\tilde{\phi_1^i}\right)\delta\left(\tilde{\phi_2^i}\right)\delta\left(\tilde{\phi_3^i}\right)|\nabla\tilde{\phi}_1^i \times \nabla\tilde{\phi}_2^i \cdot \nabla\tilde{\phi}_3^i|\mathrm{d}x\right) \\ + \sum_j \left(\int \tilde{T}_P\delta(\psi_1^j)\delta(\psi_2^j)\delta(\psi_3^j)|\nabla\psi_1^j \times \nabla\psi_2^j \cdot \nabla\psi_3^j|\mathrm{d}x\right) \end{array}\right\} \text{in 3D} \end{array}\right\}.\end{aligned} \tag{11}$$

The above cost function is always non-negative, and the symmetric nature of the cost function ensures exact matching when the cost function is minimized to 0. Moreover, the minimum of the cost function in Eq. (11) is achieved with exact matching regardless of the action of h

on the deformed distance function $\tilde{T}_P$, although re-initialization of $\tilde{T}_P$ to the distance function of the displaced points $\tilde{P}^i$'s will have numerical advantages. Also notice that landmark point matching is a special case of Eq. (11) as in this case; the anatomic structures are single points and the distance function involved is the Euclidian distance to the points.

For the level-set functions involved in Eq. (11), the following choice is proposed

$$\tilde{\phi}^i_n(x) = x_n - \tilde{p}^i_n = x_n - \left(p^i_n - u^{-1}_n(P^i)\right);$$
$$\psi^j_n(x) = x_n - q^j_n. \tag{12}$$

The advantage of the choice Eq. (12) is that now the gradient vectors of $\tilde{\phi}_1$, $\tilde{\phi}_2$, ψ^j_1 and ψ^j_2 become unit vectors pointing in the x_1 and x_2 direction, respectively. With this simplification, the body force vector in Eq. (5) (Eq. (10) in the 3D case) can be expressed in terms of components in the x_1 and x_2 direction given by

$$\sum_i \left(-\tfrac{\partial T_Q}{\partial x_1}\delta(\tilde{\phi}_1 i)\delta(\tilde{\phi}_2 i)\right) + \sum_j \left(-\tfrac{\partial \tilde{T}_P}{\partial x_1}\delta(\psi^j_1)\delta(\psi^j_2)\right);$$
$$\sum_i \left(-\tfrac{\partial T_Q}{\partial x_2}\delta(\tilde{\phi}_1 i)\delta(\tilde{\phi}_2 i)\right) + \sum_j \left(-\tfrac{\partial \tilde{T}_P}{\partial x_2}\delta(\psi^j_1)\delta(\psi^j_2)\right). \tag{13}$$

In the case of 3D, the x_1 component of the body force becomes

$$\sum_i \left(-\frac{\partial T_Q}{\partial x_1}\delta(\tilde{\phi}^i_1)\delta(\tilde{\phi}^i_2)\delta(\tilde{\phi}^i_3)\right) + \sum_j \left(\frac{\partial \tilde{T}_P}{\partial x_1}\delta(\psi^j_1)\delta(\psi^j_2)\delta(\psi^j_3)\right). \tag{14}$$

The x_2 and x_3 components of the body force in 3D are similarly defined.

Notice that Eqs. (13) and (14) can be interpreted as moving the discretized points along the gradient of the other anatomic structure's distance function. By using the following approximated delta function with support λ equal to the grid size, we smear the body force in Eqs. (13) and (14) onto the neighboring 4 grid points in 2D (8 grid points in 3D)

$$\delta_\lambda(x) = \left\{ \begin{array}{cc} \left(1+\cos\left(\frac{x\pi}{\lambda}\right)\right)/2\lambda & |x|\le\lambda \\ 0 & |x|>\lambda \end{array} \right\} \tag{15}$$

Also notice that no level-set function has to be computed explicitly as they are analytically defined given the position of $\tilde{P}^i$ as in Eq. (12). In practice, we implement Eqs. (13) and (14) by incorporating the inverse consistency approach proposed in Christensen and Johnson (2001) along with the linear elastic operator for regularizing the displacement u. This ensures that matching any image A to image B generates the same point correspondences as would be achieved by matching image B to image A.

Geometric feature matching using large deformation models

The large deformation models, as first introduced in Christensen et al. (1996), utilize formulations borrowed from fluid dynamics and continuum mechanics in order to rigorously define mappings that ensure diffeomorphisms (i.e., smooth one-to-one maps that do not tear or fold). Coupling our proposed approach with large deformation models best illustrates the power of the hybrid implicit/explicit image warping techniques as the implicit representations allow us to convert feature constraints into common integral forms. In this paper, we incorporate our method into one of the recently developed large deformation models: the large deformation diffeomorphic metric mapping (LDDMM) proposed in Miller et al. (2002). This model can be viewed as an extension of the large deformation fluid matching of Christensen et al. (1996), resulting in rigorously defined geodesics (i.e., shortest paths) linking anatomic images. To summarize this approach, the source image is carried by a forward time-dependent flow (denoted by g) that is modeled by an Euler transport equation equipped with a velocity field v: $(\partial g/\partial t) = v(g(x,t),t)$. Here, time t is defined on the unit interval [0,1]. The matching is enforced at $t = 1.0$ and thus $g^{-1}(x,t)$ is equivalent to the notation h in previous sections. We now propose the following minimization problem (Eq. (16)) by coupling our proposed framework with LDDMM. With regularization on the velocity field v as shown in Eq. (16), it has been proved that the minimizer ensures diffeomorphic mappings under minor restrictions on the differential operator L (refer to Dupuis et al., 1998; Miller, 2004; Trouve, 1998):

$$\min_v \left\{ \int_0^1 \int_\Omega \langle Lv(x,t), Lv(x,t)\rangle \mathrm{d}x\mathrm{d}t + \sum_i T_Q\left(P^i|_{g(x,1)}\right) + \sum_j T_p\left(Q^j|_{g^{-1}(x,1)}\right)\right\} \tag{16}$$

Here the flows are integrated on the space–time element $\Omega \times [0,1]$, and <,> denotes the Hilbert space inner product. Notice that omitting either one of the two matching terms in Eqs. (11) and (16) results in partial matching of the structures. The difference between Eq. (16) and

Eq. (11) is that, with explicit modeling of the forward and backward path in Eq. (16), we enforce perfect matching by comparing the target structure to the warped source structure under the forward map at time 1.0, and the source structure to the warped target structure under the backward map at time 1.0. Thus, distance functions are no longer deformed as in the second matching term in Eq. (11), resulting in a more symmetric matching cost functional.

Now we rewrite the matching term in Eq. (16) using Eqs. (1) and (8) with the short notations $g_1 = g\ (x,t)$ and $g_1^{-1} = g^{-1}\ (x,t)$

$$\sum_i T_Q\left(P^i|_{g(x,1)}\right) + \sum_j T_P\left(Q^j|_{g^{-1}(x,1)}\right) = \begin{cases} \sum_i \int T_Q \delta\left(\phi_1^i \circ g_1^{-1}\right)\delta\left(\phi_2^i \circ g_1^{-1}\right)\left|\nabla\left(\phi_1^i \circ g_1^{-1}\right) \times \nabla\left(\phi_2^i \circ g_1^{-1}\right)\right|dx \\ \quad + \sum_j \int T_P \delta\left(\psi_1^j \circ g_1\right)\delta\left(\psi_2^j \circ g_1\right)\left|\nabla\left(\psi_1^j \circ g_1\right) \times \nabla\left(\psi_2^j \circ g_1\right)\right|dx & \text{in 2D} \\ \sum_i \int T_Q \delta\left(\phi_1^i \circ g_1^{-1}\right)\delta\left(\phi_2^i \circ g_1^{-1}\right)\delta\left(\phi_3^i \circ g_1^{-1}\right)\left|\nabla\left(\phi_1^i \circ g_1^{-1}\right) \times \nabla\left(\phi_2^i \circ g_1^{-1}\right)\cdot\nabla\left(\phi_3^i \circ g_1^{-1}\right)\right|dx & \\ \quad + \sum_j \int T_P \delta\left(\psi_1^j \circ g_1\right)\delta\left(\psi_2^j \circ g_1\right)\delta\left(\psi_3^j \circ g_1\right)\left|\nabla\left(\psi_1^j \circ g_1\right) \times \nabla\left(\psi_2^j \circ g_1\right)\cdot\nabla\left(\psi_3^j \circ g_1\right)\right|dx & \text{in 3D} \end{cases}. \tag{17}$$

The first matching term, when expressed in integral form, is in the form $\sum_i \int F\left(T_Q(x), \Phi^i \circ g^{-1}(x,1)\right)dx$ with F denoting a general functional relation (the dual form $\sum_i \int F\left(T_P(x), \Psi^j \circ g(x,1)\right)dx$ for the second term) that shares a similar structure with the intensity least square cost functional $||T(x) - S(g^{-1}(x,1))||^2$ as both involve $g^{-1}(x,t)$. The least-square cost functional has the following gradient descent direction via its Euler–Lagrange equation (Miller et al., 2002) with the notations $g_1 g_t^{-1} = g(g^{-1}(\cdot,t),1)$ and D the Jacobian operator

$$-\left(S\left(g^{-1}(x,t)\right) - T\left(g_1 g_t^{-1}(x)\right)\right)\nabla S\left(g^{-1}(x,t)\right)D\left(g^{-1}(x,t)\right)\left|Dg_1 g_t^{-1}(x)\right|. \tag{18}$$

The gradient descent direction given by the first matching term $\sum_i T_Q\left(P^i|_{g(x,1)}\right)$ in Eq. (17) can be derived similarly (see Liao, 2003 for details) using the notation in Eq. (6)

$$\sum_i \left\{ \prod_n \delta\left(\phi_n^i \circ g^{-1}(x,t)\right) \times \sum_n f_n\left(T_Q \circ g_1 g_t^{-1}, \Phi^i \circ g^{-1}(x,t)\right)\nabla\left(\phi_n^i \circ g^{-1}(x,t)\right)\right\}\left|Dg_1 g_t^{-1}\right|. \tag{19}$$

Here $\nabla\ (\phi_n^i \circ g^{-1}(x,t)) = \nabla\phi_n^i(g^{-1}(x,t))Dg^{-1}(x,t)$.

In Appendix C, we derive the gradient descent direction contributed by the second matching term $\sum_j T_P\left(Q^j|_{g^{-1}(x,1)}\right)$. Collecting terms in Eq. (19) and Appendix C, we thus obtain the Euler–Lagrange equation of Eq. (16) for all t in [0,1]

$$\begin{aligned} &L^+Lv(x,t) + \sum_i \left\{ \prod_n \delta\left(\phi_n^i \circ g^{-1}(x,t)\right) \right. \\ &\quad \left. \times \sum_n f_n\left(T_Q \circ g_1 g_t^{-1}, \Phi^i \circ g^{-1}(x,t)\right)\nabla\left(\phi_n^i \circ g^{-1}(x,t)\right)\right\}\left|Dg_1 g_t^{-1}\right| \\ &\quad - \sum_j \left\{ \prod_n \delta\left(\psi_n^i \circ g_1 g_t^{-1}\right) \sum_n f_n\left(T_P \circ g^{-1}(x,t), \Psi^j \circ g_1 g_t^{-1}\right)\nabla\left(\psi_n^j \circ g_1 g_t^{-1}\right)\right\}\left|Dg^{-1}(x,t)\right| = 0. \end{aligned} \tag{20}$$

Here L^+ is the adjoint operator of L. The term L^+Lv can be viewed as generalized momentum, and thus Eq. (20) denotes the momentum equation at any given time t (see Holm et al., 2004; Miller, 2004 for more discussions on momentum). Moreover, the momentum is also conserved under the mathematical construction in Miller (2004), and the path linking any two structures can be determined by the initial momentum at $t = 0$

$$\begin{aligned} &-\sum_i \left\{ \prod_n \delta\left(\phi_n^i\right) \sum_n f_n\left(T_Q \circ g(x,1), \phi^i\right)\nabla\left(\phi_n^i\right)\right\}\left|Dg(x,1)\right| \\ &+\sum_j \left\{ \prod_n \delta\left(\psi_n^i \circ g(x,1)\right) \sum_n f_n\left(T_P, \Psi^j \circ g(x,1)\right)\nabla\left(\psi_n^i \circ g(x,1)\right)\right\}. \end{aligned} \tag{21}$$

We now proceed to simplify Eq. (20) that allows us to convert back and forth between explicit and implicit formulations. With the notation $g_t g_1^{-1} = g(g^{-1}(x,1),t)$ denoting the inverse mapping of $g_t g_1^{-1}$, we observe that $\Pi_n \delta\left(\phi_n^i g^{-1}(x,t)\right)$ and $\Pi_n \delta$

$\left(\psi_n^j \circ g_1 g_t^{-1}\right)$ can be viewed as point sources at $P^i|_{g(x,t)}$ and $Q^j|_{g_t g_1^{-1}}$. Let the notation $[g^{-1}(x,t)]_n$ be the nth coordinate component of the map $g^{-1}(x,t)$ (similarly for other bracket notations), we propose the following choice of the level-set functions

$$\begin{aligned}
&\phi_n^i(x) = x_n - p_n^i;\\
&\phi_n^i \circ g^{-1}(x,t) = \left[g^{-1}(x,t)\right]_n - p_n^i;\\
&\psi_n^j(x) = x_n - q_n^j;\\
&\psi_n^j \circ g_1 g_t^{-1} = \left[g_1 g_t^{-1}\right]_n - q_n^j;\\
&\nabla\left(\phi_n^i \circ g^{-1}(x,t)\right) = \nabla\left[g^{-1}(x,t)\right]_n;\\
&\nabla\left(\psi_n^j \circ g_1 g_t^{-1}\right) = \nabla\left[g_1 g_t^{-1}\right]_n.
\end{aligned} \tag{22}$$

By comparing Eq. (6) with Eqs. (5) and (10), we notice that the components f_n depend only on the gradient of the level-set functions. With Eq. (22), the gradient vectors of the level-set functions are independent of the positions of P^i and Q^j. Thus, each component f_n in Eq. (20) becomes independent of the position of the points and thus the level-set functions, and depends only on $Dg^{-1}(x,t)$ or $Dg_1 g_t^{-1}$.

We now rewrite the terms in Eq. (20) using Eq. (22) into the following alternative form without involving explicitly the level-set functions.

$$\sum_i \left\{\delta\left(P^i|_{g(x,t)}\right)\sum_n f_n\left(T_Q \circ g_1 g_t^{-1}, Dg^{-1}(x,t)\right)\nabla\left[g^{-1}(x,t)\right]_n\right\}\left|Dg_1 g_t^{-1}\right| - \sum_j \left\{\delta\left(Q^j|_{g_t g_1^{-1}}\right)\sum_n f_n\left(T_P \circ g^{-1}(x,t), Dg_1 g_t^{-1}\right)\nabla\left[g_1 g_t^{-1}\right]_n\right\}\left|Dg^{-1}(x,t)\right|. \tag{23}$$

Let us lastly examine in detail the functional similarity of the components f_n in 2D and 3D under Eq. (22). Given any scalar function $G(x)$, and 3D vectors v_1, v_2, and v_3, we first define the following vector-valued operator

$$V(G, v_1, v_2, v_3) \equiv \left\{\begin{array}{ll} G\cdot(v_2 \times v_3) & \text{if } v_1\cdot(v_2 \times v_3) \geq 0\\ -G\cdot(v_2 \times v_3) & \text{otherwise}\end{array}\right\}. \tag{24}$$

Given any mapping h: $\Omega \rightarrow \Omega$, the components f_n in Eq. (23) in the 3D case can be obtained by plugging Eq. (22) into Eq. (10)

$$\begin{aligned}
&f_1(G, Dh) = \mathrm{div}(V(G, \nabla h_1, \nabla h_2, \nabla h_3));\\
&f_2(G, Dh) = \mathrm{div}(V(G, \nabla h_2, \nabla h_3, \nabla h_1));\\
&f_3(G, Dh) = \mathrm{div}(V(G, \nabla h_3, \nabla h_1, \nabla h_2)).
\end{aligned} \tag{25}$$

Here h_1, h_2, and h_3 are the x, y, and z components of the mapping h. In 2D, the components f_n can also be similarly expressed in terms of the operator V by plugging Eq. (22) into Eq. (5)

$$\begin{aligned}
&f_1(G, Dh) = \mathrm{div}(V(G, \nabla h_1, \nabla h_2, \omega_3));\\
&f_2(G, Dh) = \mathrm{div}(V(G, \nabla h_2, \nabla h_1, \omega_3)).
\end{aligned} \tag{26}$$

Here the gradient vectors of h_1 and h_2 are extended to 3D by appending zero in the z-dimension, and ω_3 denotes the unit vector (0, 0, 1) pointing in the z direction.

Lastly, let us comment briefly on the choice of the sign in Eq. (24). We notice that the mixed product when evaluating Eq. (24) only becomes zero when the grid undergoes self-crossing, and thus the sign choice never changes under diffeomorphic mappings. It is easy to check that under common x–y–z convention, the sign choice in the 3D case when calculating f_1, f_2, and f_3 in Eq. (25) at initialization [i.e., $g^{-1}(x,t)$ and $g_1 g_t^{-1}$ are both the identity map] always evaluates to the first condition in Eq. (24). In 2D, the components f_1 and f_2 in Eq. (26) evaluates to the first and second condition in Eq. (24), respectively.

Results and discussion

In this section, we first validate the proposed matching method under large-deformation model as introduced in Eqs. (16) and (17) by comparing 2D curves extracted from sulcal traces in normal healthy subjects. To motivate this application, we note that surface-based 3D models of the human cortex are often extracted from brain MRI scans and flattened onto a 2D plane or other 2D surface such as a sphere, for subsequent visualization and analysis (Hurdal and Stephenson, 2004; Sereno et al., 1996; Thompson et al., 2004;

van Essen, 2004). If sulcal features are flattened as well, one application is to align these sulcal features across subjects before integrating functional or structural data from many subjects (Zeineh et al., 2003). In group studies of the cortex, this reduces some of the confounding variance caused by gyral patterning differences among individuals. The central sulcal trace from one normal subject was delineated and flattened to the 2D cortical parameter space as described in Thompson and Toga (2002). The individual central sulcus, represented as a flat 2D curve, was then warped to an average central sulcus of 31 healthy normal subjects in the parameter space. The curve was parameterized and uniformly discretized to 100 points. The alignment computation was performed in a 64 × 64 × 11 cube with the smoothing operator $(-0.01\Delta + \mathrm{id})^2$. Here the spatial domain is gridded at 64 × 64 sampling and 11 time points are considered in the range [0,1]. The two curves were matched using either pair-wise point matching (homothetic mapping) or whole curve matching by treating the curve as a single anatomic structure. In a homothetic mapping, two curves are first parameterized at uniform speed using 100 equally spaced points, and each point is matched with its counterpart in the 100 point sequence. In whole-curve matching, it is only required that overall one curve be matched to the other, and a higher-order matching of specific internal points is not explicitly enforced. Furthermore, unidirectional point and whole curve matching were also used for comparison by dropping the second matching term in Eq. (16), i.e., minimizing the following cost functional instead

$$\min_v \left\{ \int_0^1 \int_\Omega \langle Lv(x,t), Lv(x,t)\rangle \mathrm{d}x\mathrm{d}t + \sum_i T_Q\left(P^i|_{g(x,1)}\right) \right\}. \tag{27}$$

Thus, a total of four different matching strategies were used including the unidirectional point and whole curve matching and the symmetric point and whole curve matching. Figs. 1 and 2 show the time path generated by four different algorithms linking the average to the individual curve. Figs. 1(a),(c) and 2(a),(c) are the paths at time 0.5, and Figs. 1(b),(d) and 2(b),(d) the path at time 1.0 with the dashed line being the average curve, dotted line the individual curve, and solid line the warped average curve under the path at current time. Figs. 1(a) and (b) show the result of symmetric point matching, Figs. 1(c) and (d) the result of symmetric curve matching, Figs. 2(a) and (b) the result of unidirectional point matching, and Figs. 2(c) and (d) the result of unidirectional curve matching. Table 1 summarizes the registration error in terms of grid sizes at these 100 discretized positions. Since a forward mapping path from the average to the individual curve and a backward

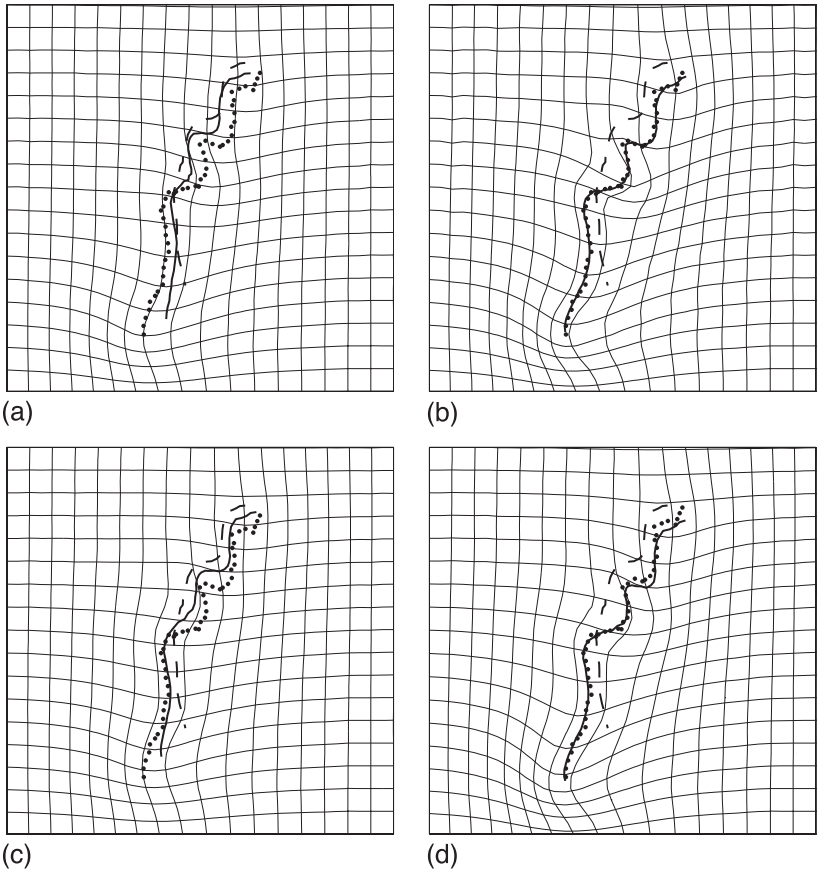

Fig. 1. An example of curve matching under large deformation symmetric point matching and large deformation symmetric whole-curve matching. This figure shows the source average curve (dashed line), target individual curve (dotted line), and warped source curve (solid line) under the deformation path at time 0.5 in (a) and (c), and time 1.0 in (b) and (d). (a) and (b) show the deformation generated using large deformation symmetric point matching while (c) and (d) show the deformation generated using large deformation whole curve matching. Notice the difference in both the geodesic path [(a) vs. (c)] and the final deformation field [(b) vs. (d)]. The matching accuracy is visually indistinguishable between these two methods.

Table 1
Error analysis for the matching results in Figs. 1 and 2

	Minimum error	Maximum error	Mean error	Standard deviation
Unidirectional point matching				
Backward error	0.0387	0.6413	0.2133	0.1450
Forward error	0.0431	0.7941	0.2437	0.1622
Symmetric point matching				
Backward error	0.0108	0.3818	0.1470	0.0933
Forward error	0.0165	0.5302	0.1893	0.1057
Unidirectional whole curve matching				
Backward error	0.0334	5.3712	0.6886	1.1927
Forward error	0.0240	0.5551	0.1542	0.1133
Symmetric whole curve matching				
Backward error	0.0027	0.3878	0.1111	0.0824
Forward error	0.0105	0.4319	0.1384	0.0829

mapping path from the individual back to the average curve were generated, errors were calculated and reported in two directions in Table 1. The forward error was evaluated by comparing the individual curve with the warped average curve under the path at time 1 and the backward error by comparing the average curve with the warped individual curve at time 1. In the case of point matching, registration error was calculated by evaluating the pairwise Euclidean distance after warping at these 100 positions. In the case of whole curve matching, the registration error was calculated by evaluating the distance function of one curve at the warped 100 discretized positions of the other curve under the corresponding path at time 1.

Visually, the registration accuracy is indistinguishable between Figs. 1(b) and (d) while quantitatively the registration error is slightly smaller in the case of whole curve matching as shown in Table 1 (mean forward error 0.1384 vs. 0.1893). Moreover, the deformation path and the final deformation at time 1 are different between the two approaches. We next compare the unidirectional and symmetric point matching technique. While in theory, point matching can be achieved without the symmetric terms introduced in Eq. (16), in practice we do notice better accuracy when the symmetric term is present as illustrated in Fig. 2. Notice the larger registration error at sharp turns of the individual sulcal curve in unidirectional point matching (Fig. 2(b)). This larger registration error is also reflected in Table 1 with a mean forward error of 0.2437 compared to 0.1893 in the case of symmetric point matching.

Lastly, as discussed in "Theory and methods", unidirectional whole curve matching may result in partial matching. In Fig.

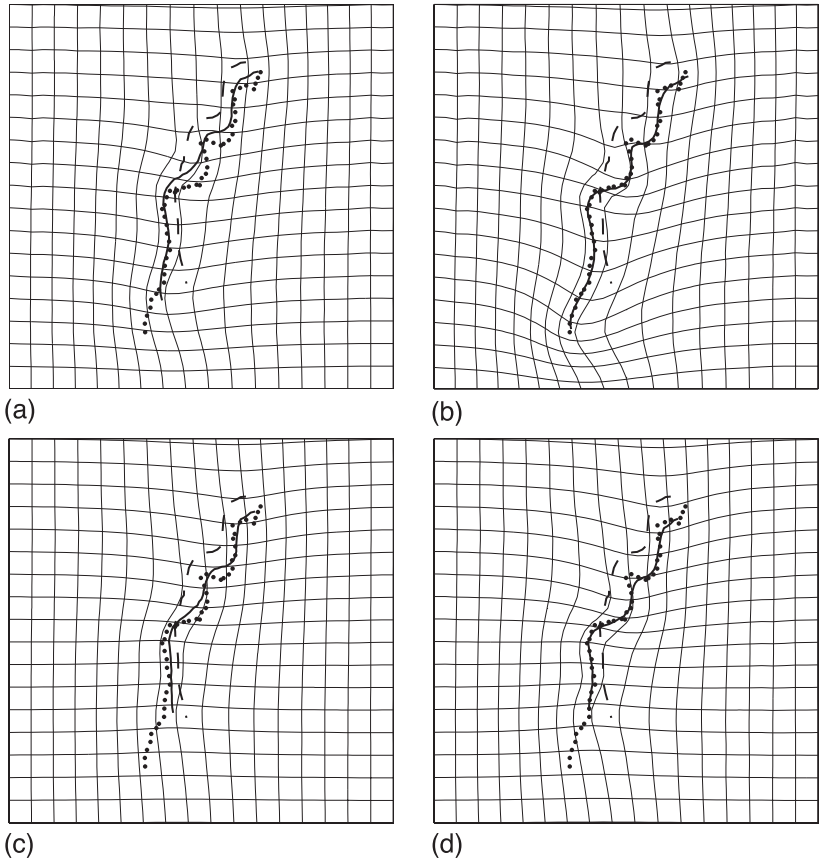

Fig. 2. An example of curve matching under large deformation unidirectional point matching and large deformation unidirectional whole curve matching. This figure shows the source average curve (dashed line), target individual curve (dotted line), and warped source curve (solid line) under the deformation path at time 0.5 in (a) and (c), and time 1.0 in (b) and (d). (a) and (b) show the deformation generated using large deformation unidirectional point matching while (c) and (d) show the deformation generated using large deformation unidirectional whole curve matching. In the case of unidirectional point matching, the matching is less accurate at sharp turns of the target curve than symmetric point matching in Fig. 1. In the case of unidirectional whole curve matching, the source curve is matched only to a subset of the target curve due to the lack of a symmetric matching term.

2(d), the warped average curve only recovers part of the individual curve (the lower end of the individual curve was not matched) with noticeable registration error at the sharp turns of the individual curve as well. This mismatch is also noted in Table 1 with a maximum backward error of 5.3712. This is because the lower end of the individual curve falls outside the average curve when pulled back by the backward mapping path at time 1.

We next tested the large deformation symmetric shape (contour) matching using a set of corpus callosum contours from subjects clinically diagnosed with autism, and a set of healthy controls. Morphometric studies of the corpus callosum have been an active area of research due to its importance in interhemispheric communication (see Thompson et al., 2003a,b for a review of these studies), and its abnormalities in callosal shape observed in many neuropsychiatric disorders including schizophrenia (Narr et al., 2000, 2002), Alzheimer's disease (Davatzikos and Resnick, 1998; Davatzikos et al., 1996a; Thompson et al., 2000a,b), fetal alcohol syndrome (Sowell et al., 2001), and autism (Chung et al., 2004; Vidal et al., 2003). In these studies, the midsagittal contour of the corpus callosum is typically traced in 2D, represented as a parametric curve, and matched to a control average curve, to identify regional shape differences or shape changes over time (Narr et al., 2002; Thompson et al., 2000a,b). Although there are few true landmarks on the corpus callosum at midline, one approach has matched callosal outlines subject to point constraints placed at the anterior and posterior limits of the contour (the rostrum and genu; marked by the four arrows in Fig. 3) while allowing sliding in the sections between them (other constraints are possible; this matching was chosen so that endpoints were associated across subjects). Therefore, in this example, two types of matching constraints are needed including the contour matching in the top and bottom middle sections, and landmark point constraints at the anterior and posterior limits. Thus, we tested this matching task to demonstrate the ability of the proposed method to handle combined constraints. The results are shown in Fig. 3 where the source contour (solid blue line) is warped to match the target contour (red dotted line) with the final warped source contour marked by dotted blue line. The anterior and posterior landmark points on the source and target curves are marked by arrows. Notice the almost exact matching at the anterior and posterior landmark points on the target contour (the matching at the anterior landmark is visually exact such that the red dot representing the anterior landmark of the target is masked by the blue dot representing the warped anterior landmark point of the source contour). The forward mapping in this case has a mean error of 0.1309 mm, a maximum error of 0.3381 mm, and a standard deviation of 0.0693 mm, while the backward mapping has a mean error of 0.1344 mm, a maximum error of 0.3449 mm, and a standard deviation of 0.0601 mm.

In order to better visualize the sliding effect in the middle sections, Fig. 4(a) plots the unit length stretch/compression factor (ranging from 0.722 to 1.39 with a mean value of 0.971 and a standard deviation of 0.1824) of the mapping form the source to the target along the source contour. Notice that stretching is most significant in the front end of the anterior third and splenium of the source contour while compression is observed in the lower midbody. Fig. 4(b) plots the unit area expansion/compression

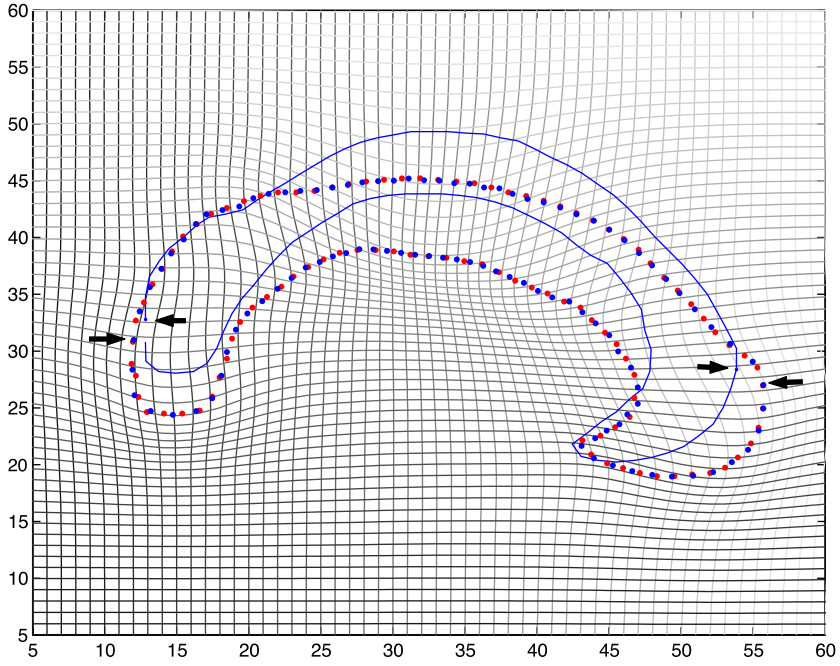

Fig. 3. An example of large deformation symmetric shape matching using corpus callosum contours from two individual autistic subjects. To ensure correct anatomic matching, the shapes are matched with strict point constraints placed at the anterior and posterior end of the contours (marked by the arrows) while allowing sliding in the middle sections. The solid blue line indicates the position of the source contour with the dotted blue line the final warped position of the source contour. The target contour is marked by dotted red line for better visualization of the sliding effect. The sliding effect is most noticeable in the lower middle section. This example illustrates the power of the proposed method where multiple constraints of different types (in this case, a contour matching coupled with point constraints) can be easily enforced.

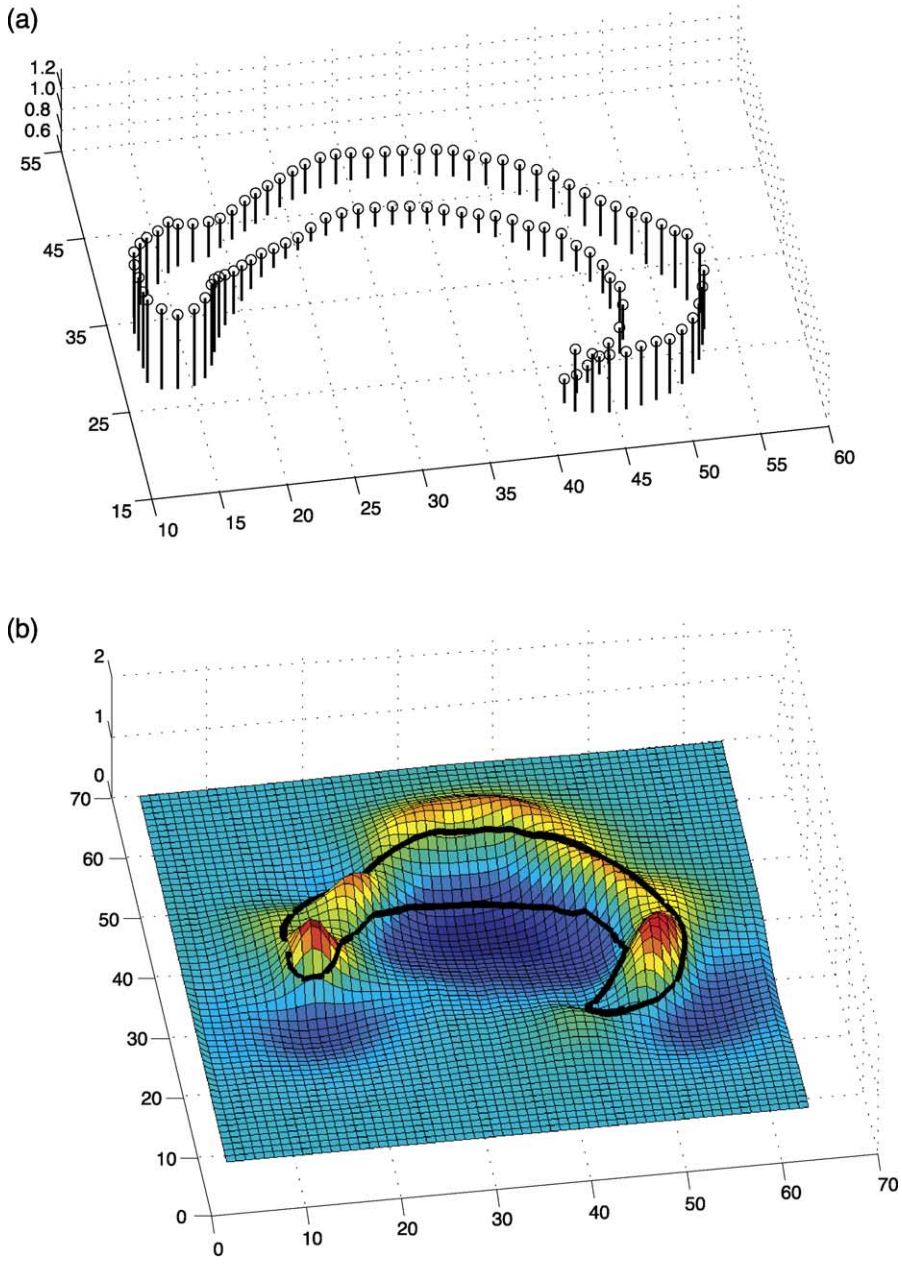

Fig. 4. Further analysis of the shape matching example in Fig. 3. (a) shows the unit length stretching/compression factor (z-axis) plotted along the boundary of the source contour. (b) shows the Jacobian (z-axis) indicating local unit area expansion/compression in a neighborhood of the source corpus callosum contour (solid black line). Both the stretching and the tissue expansion are most prominent in the anterior third and the splenium regions of the contour.

factor (here ranging from 0.441 to 1.9429 with a mean value of 1.001) in a neighborhood of the source contour where tissue expansion is again noted in similar regions of the source contour. The results are consistent with human visual perceptions as the middle section of the source contour in Fig. 3 has to be squeezed downward to match the corresponding section of the target contour, while the anterior and posterior parts of the target contour are substantially larger in size.

In contrast, the unit length stretch/compression factor will be constant along the contour if the matching is achieved by homothetic mapping via a landmark point matching method. This creates a discrepancy between the Jacobian plot and the unit length stretch/compression factor as the area where tissue is being compressed or expanded still has a constant boundary stretch/compression factor. Thus, contour matching via homothetic point matching yields relatively unnatural mapping in the sense that the homothetic mapping of the boundary and the tissue volume/area change are inconsistent. This is important consideration when warping is used to study growth and degeneration, as the regularization operator used will have some impact on the overall profile and spatial uniformity of the measured growth (homothetic mapping essentially corresponds to using the covariant Laplacian operator restricted to the curves, when matching 2D curves; Thompson et al., 2000a,b).

We next demonstrate the use of this method in tensor-based morphometry using 20 normal control and 20 autistic patients. Corpus callosum outlines were derived from T1-weighted 3D MP-RAGE MRI volumes (1.2-mm isotropic resolution) acquired at 3.0-T (IMRIS, Winnipeg, Canada) from autistic children (mean age: 9.35 years ± 3.27 SD) and healthy controls (10.15 years ± 2.11SD), matched for age, height, sex, and other demographic criteria. Scans were normalized by affine transformation to ICBM standardized stereotaxic space (Mazziotta et al., 2001). To establish a reference shape, an average contour was first generated by averaging the coordinates of the discretized contours of the 20 control subjects. In the next step, the average contour was warped using the proposed level-set-based approach to each subject in both the autistic and control group. The local Jacobian plot for each individual was then calculated based on the corresponding deformation field (note that the Jacobian of a mapping is a positive number expressing the areal dilation of the warping field—numbers above 1 denote expansion, while numbers below 1 denote compression; see Thompson et al., 2000a,b for examples). The top panel of Fig. 5 shows the mean log(Jacobian) plot of the control group while the lower panel shows the same plot of the autistic group. By convention, Jacobian values are typically subjected to log transformation before comparison, to make them more normally distributed, as the deformation tensor Lie group is a Riemannian manifold that can be flattened using a log transformation (Pennec et al., 2004; Woods, 2003). Regions with Jacobian below 1 [i.e., negative log(Jacobian)—or tissue loss] in the autistic group are observed in the genu and the splenium of the corpus callosum, consistent with prior findings of callosal thinning

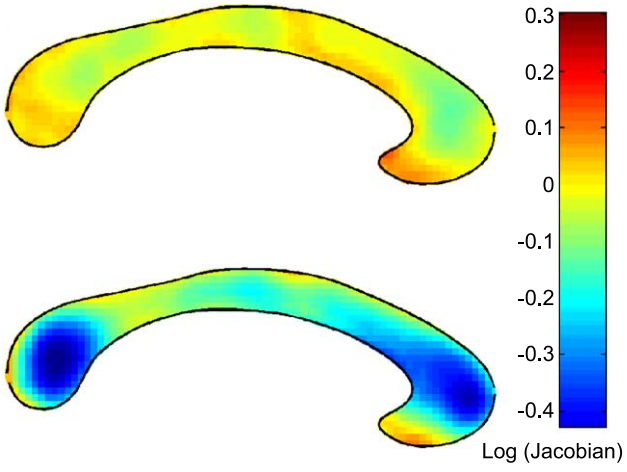

Fig. 5. This figure shows the mean log(Jacobian) plots of the control (N = 20) and the autistic (N = 20) group. An average contour was first generated by averaging the coordinates of the discretized contours of the control subjects. The Jacobian for each individual in both the control and autistic group is then calculated by mapping the average contour to this individual subject. Top panel shows the mean log(Jacobian) plot of the control group while the lower panel shows the same plot of the autistic group. Regions with negative Jacobian (tissue deficits) in the autistic group is noticeable in the genu and the splenium of the corpus callosum. Finally, as would be expected, the mean log(Jacobian) of the controls to the control average mesh is approximately zero. It is not identically zero as the mean callosal curve was created by averaging curves in Euclidean space (Narr et al., 2002; Thompson et al., 2000a,b), whereas the Jacobian measures the average, or expected value, of the areal expansion required to match this curve. For a given matching operator L, there may be no such curve for which this expectation map is uniformly zero.

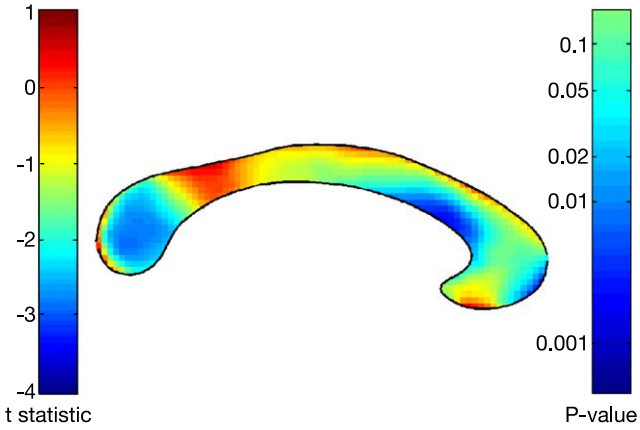

Fig. 6. This figure plots the t-statistics and the corresponding P values calculated based on the log(Jacobian) values obtained from the control and the autistic group. The t-statistic is computed by performing a t test, at each pixel, of the log(Jacobian) values under the null hypothesis that there is no mean shape difference between the groups. The corresponding P value is shown on the right color bar. Notice the relatively significant differences in the splenium and also some parts of the genu–truncus junction of the corpus callosum. This figures demonstrates the use of the proposed method in tensor-based morphometry.

in this area (Vidal et al., 2003). In order to assess the significance of difference between the control and the autistic group, we performed a pixel-wise t test on the log(Jacobian) values obtained from the two groups under the null hypothesis that autistic and control subjects share a common mean log(Jacobian) value (following prior work by Chung et al., 2001; Davatzikos et al., 1996a). The t-statistics along with the corresponding P values (under a null t distribution with 38 degrees of freedom) are shown in Fig. 6 where possible tissue loss is noted mainly in the splenium area. The results are consistent with the findings from previous studies (Vidal et al., 2003), and demonstrate potential applications of the proposed framework to tensor-based morphometry in computational anatomy (Ashburner et al., 1998; Chung et al., 2001; Davatzikos et al., 1996a; Pettey and Gee, 2001; Studholme et al., 2004; Thompson et al., 2000a,b). Further work is necessary to establish the cognitive or clinical correlates of these findings, if any, but here we note that regional differences are likely to be localized quite effectively using the mapping approach. In the future, we will apply the proposed method to a larger data set to confirm the localization of the deficits. Lastly, notice that a simple Euclidean average was used to obtain the average corpus callosum contour in this example. Averaging using large-deformation models and related geodesic PCA techniques (Avants and Gee, 2004; Vaillant et al., 2004) is a new and emerging field and much interesting research is currently underway. It is also our intention to explore geodesic averages for geometric features as well as nonlinear averaging methods based on the proposed matching framework by allowing sliding.

We next apply the proposed method to brain surface mapping and investigate its impact on the computation of deformation fields that match cortical anatomy across subjects and subsequent statistical analysis of brain surfaces. Brain surfaces from 20 normal health young adults were extracted from high-resolution MRI scans as described previously (Thompson et al., 2004). For each subject, 23 sulci/control lines per hemisphere were traced using a standard anatomical protocol (Sowell et al., 2001; Thompson et al., 2003a,b) described on the Internet at http://www.loni.ucla.edu/

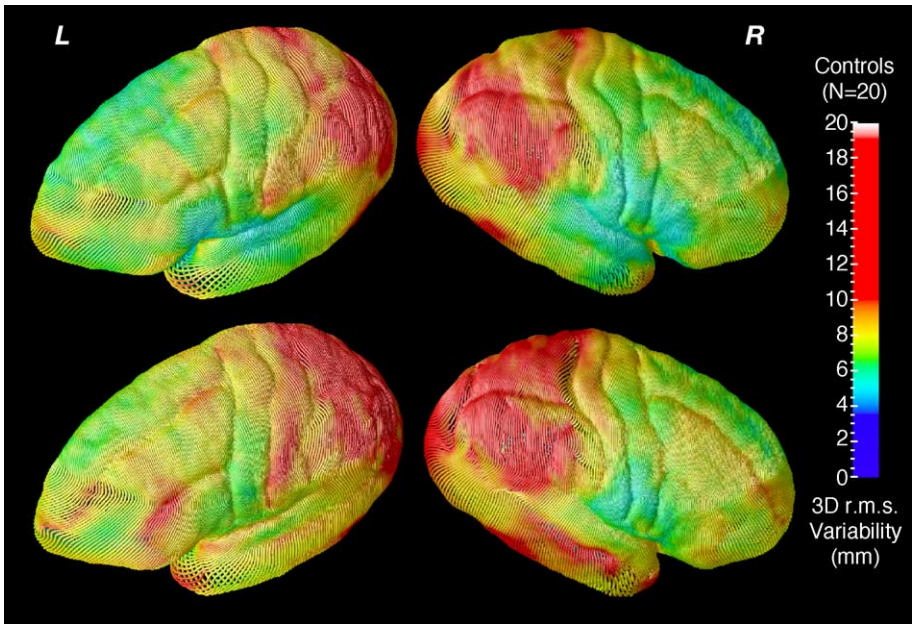

Fig. 7. Variability maps of 20 normal control subjects generated using two different approaches. The top panel shows the maps based on the level-set matching approach proposed in this paper, while the lower panel shows the same maps based on the approach currently employed in our lab (Thompson and Toga, 1997; Thompson et al., 2000a,b). The color bar indicates patterns of variability in each group as the root mean square magnitude of displacement vectors from each individual to the group average surface, at each surface point on the brain hemisphere. Greatest anatomic variability is observed in the parietal cortices in both hemispheres consistent with previous findings (Thompson et al., 2000a,b). The level-set method proposed in this paper visually reduces the variability in most parts of both the left and right hemispheres. The reduced variability is due to the fact that, by allowing sliding along the curves, the brain surfaces are warped, allowing adjustment of the point correspondences along the curves such that a warping field with less distortion can be reached.

NCRR/Downloads/Protocols/SulcalAnatomy.html. The brain surfaces and corresponding curve traces were then flattened to a 2D unit square parameter space discretized using a 256 × 256 grid (Thompson and Toga, 1997; Thompson et al., 1997). Sulcal features lying on the brain surface were then projected into flat space coordinates, producing a set of flattened sulcal curves for each subject. The flattened cortical surfaces were then warped in the 2D parameter space by mapping the individual traces to a set of average traces of 31 normal human subjects using the proposed approach. Left and right hemispheres were treated separately. The warping in 2D parameter space induced a new correspondence of the 3D brain surfaces among different subjects with the major sulcal variations factored out. Thus, 3D locations from different subjects at the same position on the parameter space are considered to represent the same locations on the brain surface, and the matching fields can be used to study variabilities in cortical patterning among individuals. A neuroanatomic variability map can then be constructed on the brain surface by calculating the

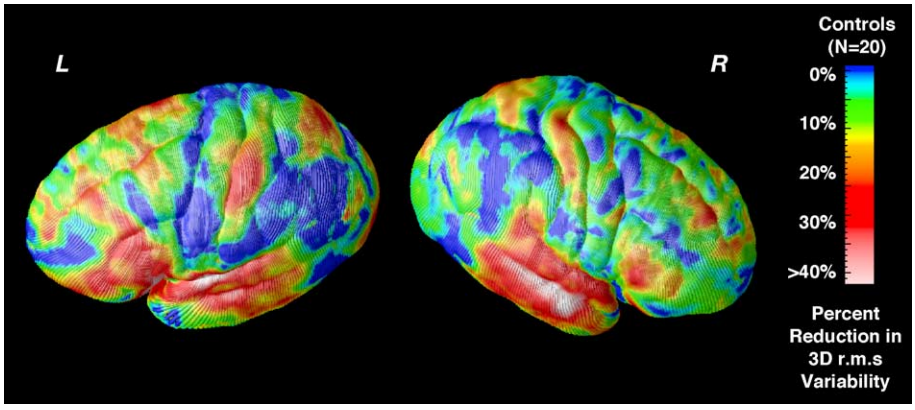

Fig. 8. Ratio images of the variability maps of 20 normal control subjects generated using two different approaches in Fig. 7. Notice the overall reduction of anatomical variability in most parts of the brain surface using the warping technique proposed in the paper. Greater reduction is observed in the temporal and also part of the frontal lobe in both hemispheres, while lesser reduction is observed in areas where greater anatomic variability is detected. This results in mappings that have less distortion while still matching homologous gyral anatomy in detail from one subject to another. In studies of gray matter density and cortical thickness, this may provide a higher signal-to-noise ratio in the maps of cortical differences and thus increased accuracy and detection sensitivity when performing statistical analysis.

RMS variability of the amplitude of the displacement vectors for the 20 subjects, matching each subject to an average surface derived for the group (see Thompson et al., 2000a,b for more details on constructing this type of variability map). Fig. 7 shows the variability maps using the proposed method for the left and right hemisphere. The variability generated by the warping method described in Thompson and Toga (1997) and Thompson et al. (1997), an implementation based on matching equally spaced points (homothetic mapping), is also shown in this figure for comparison. The proposed method visually reduces the variability in most parts of both the left and right hemispheres, with larger anatomic variability noticed in the parietal cortices of both hemispheres. The reduced variability is due to the fact that, by allowing sliding along the curves, the brain surfaces are warped to the standard space with adjustment of the point correspondences along the curves such that a less strained/deformed final configuration is reached. Moreover, by allowing sliding along the curves, other similarity cost functionals are more likely to be optimally minimized, thus achieving better registration results by letting different cost functionals work in synergy. In order to better visualize the effect of the reduction, ratio images of the variability maps generated using the two different approaches are shown in Fig. 8. Notice again the overall reduction of anatomical variability in most parts of the brain surface using the technique proposed in the paper. Greater reduction is observed in the temporal and also part of the frontal lobe in both hemispheres, while lesser reduction is observed in areas where greater anatomic variability is detected. This results in mappings that have less distortion while still matching homologous gyral anatomy in detail from one subject to another. In studies of gray matter density and cortical thickness, this may provide a higher signal-to-noise ratio in the maps of cortical differences and thus increased accuracy and detection sensitivity when performing statistical analysis. In functional imaging studies, this may also increase the detection sensitivity of the experimental design.

Discussion

In this paper, we present a novel and systematic approach for comparing anatomic structures by distance functions and hybrid implicit/explicit point representations. The final formulations eliminate explicit use of the level-set functions and can be viewed as a nontraditional level-set method in a Lagrangian reference frame. The proposed framework deals with all geometric representations of features and can be incorporated into any regularization technique that employs the gradient descent method (e.g., the linear elastic operator, large deformation fluid matching model, and the LDDMM). We extend our previous work and propose new matching cost functions that allow matching of anatomic structures without explicit constructions of the level-set functions representing them. The proposed approach thus brings together the level-set method and image warping, and offers a novel direction of research where standard level-set techniques can be transferred and applied back and forth between implicit and explicit forms. This simplifies mathematical derivations and unifies theories under a common construction and provides alternative interpretations of the traditional Eulerian level-set method.

The proposed hybrid implicit/explicit framework is relevant not only to the mathematics of nonlinear image warping but also to the theory of pattern recognition. For example, when implemented with the large deformation metric model, one geometric object can be continuously morphed to another without requiring any specific point correspondences in the whole morphing path. This significantly differs from the common practice of pattern recognition/matching via the discretization of shapes. Moreover, we can define the average of two anatomical structures to be the warped source (or target) structure at time 0.5. How this new concept of averaging differs from the concept of averaging employed by traditional pattern recognition theory is an interesting topic and will be further investigated.

Let us also point out that the cost functional proposed in Eq. (16) is one of the simplest forms that can achieve exact feature matching. For example, we can look at an alternative cost functional in Eq. (28) by raising the power of the distance function to n or other functional forms acting on the distance function (this corresponds to the use of higher-order L^p norms in functional analysis). In any case, the cost functional can always be expressed via the implicit representations for points and thus can be solved using the same framework.

$$\min\left\{\sum_i T_Q^n\left(P^i|_{g(x,1)}\right)+\sum_j T_P^n\left(Q^j|g^{-1}(x,1)\right)\right\} \tag{28}$$

Lastly, we tested the proposed framework in the tensor-based morphometry of the corpus callosum and measuring anatomic variability of normal brain surfaces. The results are promising and improve on existing methods, specifically because they can relax mappings along curved boundaries. In summary, the mathematical framework and techniques introduced in this paper are likely to be advantageous in the field of neuroimaging, and offer a new and exciting direction of research in which more flexible and robust registration techniques can be designed and different registration criteria can be unified.

Acknowledgments

This work is funded in part by NIH Grants R21 EB001561 and R21 RR019771 (to P.T.), P41 RR13642 and U54 RR021813 (to A.W.T.), DOE contract DE-FC03-02ER63420 (to S.C. Huang) and UCLA Brain Injury Research Center.

Appendix A. Proof of Eq. (1)

We first construct a shape ($PQRS$ in Fig. 9) with area ε^2 (ε a very small positive number) by extending the zero level sets of ϕ_1 and ϕ_2 (solid lines in Fig. 9) in their outer normal directions in a parallel fashion. The shape can be well approximated by a parallelogram as we let ε go to zero. We first extend the zero level set of ϕ_1 to a distance of ε away (the dashed line parallel to the zero level set of ϕ_1) from its zero level set along the outer normal direction. The value of the level-set function ϕ_1 at this new position is

$$\begin{aligned}\phi_1\left(x+\varepsilon\frac{-\nabla\phi_1}{|\nabla\phi_1|}\right) &= \phi_1(x)+\varepsilon\nabla\phi_1\cdot\frac{-\nabla\phi_1}{|\nabla\phi_1|}+O_1\left(\varepsilon^2\right)\\ &= -\varepsilon|\nabla\phi_1|+O_1\left(\varepsilon^2\right).\end{aligned} \tag{A1}$$

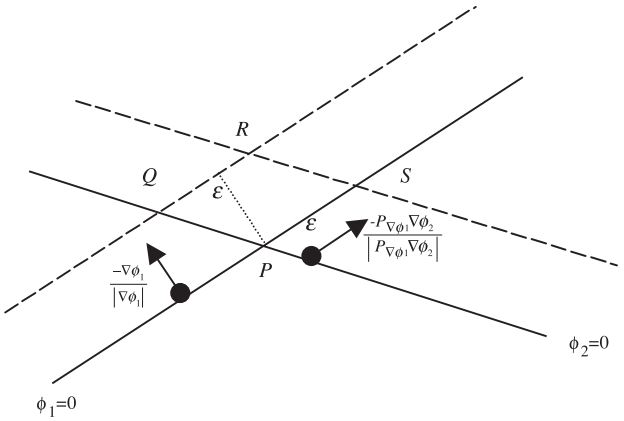

Fig. 9. An illustration of the extraction of the value of a scalar function at a point *P*. The shape *PQRS* can be approximated by a parallelogram as ε approaches zero.

In order to construct parallelogram with area ε^2, we look at the value of ϕ_2 with distance ε away from its zero level set along the tangential direction of the zero level set of ϕ_1

$$\phi_2\left(x+\varepsilon\frac{-P_{\nabla\phi_1}\nabla\phi_2}{|P_{\nabla\phi_1}\nabla\phi_2|}\right)=-\varepsilon|P_{\nabla\phi_1}\nabla\phi_2|+O_2(\varepsilon^2). \tag{A2}$$

With $\bar{G}$ the value of G averaged inside the parallelogram *PQRS*, we have the following

$$\begin{aligned}\varepsilon^2\bar{G}\cong&\int G(x)H(\phi_1(x)+\varepsilon|\nabla\phi_1|)H\big(\phi_2(x)+\varepsilon|P_{\nabla\phi_1}\nabla\phi_2|\big)\mathrm{d}x\\&-\int G(x)H(\phi_1(x))H\big(\phi_2(x)+\varepsilon|P_{\nabla\phi_1}\nabla\phi_2|\big)\mathrm{d}x\\&-\int G(x)H(\phi_1(x)+\varepsilon|\nabla\phi_1|)H(\phi_2(x))\mathrm{d}x\\&+\int G(x)H(\phi_1(x))H(\phi_2(x))\mathrm{d}x.\end{aligned} \tag{A3}$$

Here H is the Heaviside function.

Using the Taylor series expansions in Eq. (A4), we thus obtain Eq. (A5)

$$\begin{aligned}&H(\phi_1(x)+\varepsilon|\nabla\phi_1|)=H(\phi_1(x))+\varepsilon\delta(\phi_1(x))|\nabla\phi_1|+O(\varepsilon^2);\\&H\big(\phi_2(x)+\varepsilon|P_{\nabla\phi_1}\nabla\phi_2|\big)=H(\phi_2(x))\\&\qquad+\varepsilon\delta(\phi_2(x))|P_{\nabla\phi_1}\nabla\phi_2|+O(\varepsilon^2).\end{aligned} \tag{A4}$$

$$\varepsilon^2\bar{G}=\varepsilon^2\int G(x)\delta(\phi_1(x))\delta(\phi_2(x))|\nabla\phi_1||P_{\nabla\phi_1}\nabla\phi_2|\mathrm{d}x+O(\varepsilon^3). \tag{A5}$$

Dividing both sides by ε^2 and letting ε approach zero, we obtain the first equality in Eq. (1).

By switching the order of the two level-set functions, we derive the second equality in Eq. (1). The third equality holds as

$$|\nabla\phi_1||P_{\nabla\phi_1}\nabla\phi_2|=|\nabla\phi_2||P_{\nabla\phi_2}\nabla\phi_1|=|\nabla\phi_1\times\nabla\phi_2|. \tag{A6}$$

Appendix B

To simplify the derivation, we will derive the Euler–Lagrange equation of the original variational form in a Eulerian reference.

$$\begin{aligned}&\min_{\phi_1\phi_2}\int G\delta(\phi_1(x))\delta(\phi_2(x))|\nabla\phi_1||P_{\nabla\phi_1}\nabla\phi_2|\mathrm{d}x\\&\quad=\min_{\phi_1\phi_2}\int G\delta(\phi_1(x))\delta(\phi_2(x))|\nabla\phi_2||P_{\nabla\phi_2}\nabla\phi_1|\mathrm{d}x.\end{aligned} \tag{B1}$$

Before our derivation, let us point out similar formulations and derivations can be found in Burchard et al. (2001) and Cheng et al. (2002), in which Eq. (B1) computes curve length in 3D (in contrast to point values in 2D in this paper) and the resulting evolution equation is the curvature motion equation. In the following, we present a different and simpler derivation that is more consistent with the setting of this paper.

We first calculate the variation of the energy by perturbing ϕ_1 in the following way

$$\begin{aligned}&\int G\delta(\phi_1+\varepsilon\eta)\delta(\phi_2)|\nabla\phi_2||P_{\nabla\phi_2}\nabla(\phi_1+\varepsilon\eta)|\mathrm{d}x\\&=\int G\varepsilon\delta'(\phi_1)\delta(\phi_2)|\nabla\phi_2||P_{\nabla\phi_2}\nabla\phi_1|\eta\mathrm{d}x\\&\quad+\int G\delta(\phi_1)\delta(\phi_2)|\nabla\varphi_2||P_{\nabla\phi_2}\nabla\phi_1+\varepsilon P_{\nabla\phi_2}\nabla\eta|\mathrm{d}x\\&\quad+O(\varepsilon^2).\end{aligned} \tag{B2}$$

We then expand the last term in equation Eq. (B2) as follows

$$\begin{aligned}&\int G\delta(\phi_1)\delta(\phi_2)|\nabla\phi_2||P_{\nabla\phi_2}\nabla\phi_1+\varepsilon P_{\nabla\phi_2}\nabla\eta|\mathrm{d}x\\&=\int G\delta(\phi_1)\delta(\phi_2)|\nabla\phi_2|\\&\qquad\left[|P_{\nabla\phi_2}\frac{\nabla\phi_1|+\langle P_{\nabla\phi_2}\nabla\phi_1,\varepsilon P_{\nabla\phi_2}\nabla\eta\rangle}{|P_{\nabla\phi_2}\nabla\phi_1|}\right]\mathrm{d}x+O(\varepsilon^2)\end{aligned} \tag{B3}$$

Let us calculate the inner product in the numerator of the *r.h.s.* of Eq. (B3)

$$\begin{aligned}\left\langle P_{\nabla\phi_2}\nabla\phi_1,\varepsilon P_{\nabla\phi_2}\nabla\eta\right\rangle&=\varepsilon\left\langle P_{\nabla\phi_2}\nabla\phi_1,\nabla\eta\right.\\&\qquad\left.-\frac{\langle\nabla\phi_2,\nabla\eta\rangle}{|\nabla\phi|^2}\nabla\phi_2\right\rangle\\&=\varepsilon\left\langle P_{\nabla\phi_2}\nabla\phi_1,\nabla\eta\right\rangle.\end{aligned} \tag{B4}$$

The second equality holds as

$$\langle P_{\nabla\phi_2}\nabla\phi_1,\nabla\phi_2\rangle=0. \tag{B5}$$

Assuming appropriate boundary conditions, we rewrite the *r.h.s.* of Eq. (B3) by applying the divergence theorem

$$\begin{aligned}
&\int G\delta(\phi_1)\delta(\phi_2)|\nabla\phi_2|\left[|P_{\nabla\phi_2}\nabla\phi_1| + \frac{\langle P_{\nabla\phi_2}\nabla\phi_1, \varepsilon P_{\nabla\phi_2}\nabla\eta\rangle}{|P_{\nabla\varphi_2}\nabla\phi_1|}\right]\mathrm{d}x \\
&= \int G\delta(\phi_1)\delta(\phi_2)|\nabla\phi_2|\left[|P_{\nabla\phi_2}\nabla\phi_1| + \varepsilon\frac{\langle P_{\nabla\phi_2}\nabla\phi_1, \nabla\eta\rangle}{|P_{\nabla\phi_2}\nabla\phi_1|}\right]\mathrm{d}x \\
&= \int G\delta(\phi_1)\delta(\phi_2)|\nabla\phi_2||P_{\nabla\phi 2}\nabla\phi_1|\mathrm{d}x \\
&\quad - \varepsilon\int \mathrm{div}\left[G\delta(\phi_1)\delta(\phi_2)|\nabla\phi_2|\frac{P_{\nabla\phi_2}\nabla\phi_1}{|P_{\nabla\phi_2}\nabla\phi_1|}\right]\eta\mathrm{d}x \\
&= \int G\delta(\phi_1)\delta(\phi_2)|\nabla\phi_2||P_{\nabla\phi_2}\nabla\phi_1|\mathrm{d}x \\
&\quad - \varepsilon\int \delta(\phi_1)\mathrm{div}\left[G\delta(\phi_2)|\nabla\phi_2|\frac{P_{\nabla\phi_2}\nabla\phi_1}{|P_{\nabla\phi_2}\nabla\phi_1|}\right]\eta\mathrm{d}x \\
&\quad - \varepsilon\int G\delta'(\phi_1)\delta(\phi_2)|\nabla\phi_2||P_{\nabla\phi_2}\nabla\phi_1|\eta\mathrm{d}x \\
&= \int G\delta(\phi_1)\delta(\phi_2)|\nabla\phi_2||P_{\nabla\phi_2}\nabla\phi_2|\mathrm{d}x \\
&\quad - \varepsilon\int \delta(\phi_1)\delta(\phi_2)\mathrm{div}\left[G|\nabla\phi_2|\frac{P_{\nabla\phi_2}\nabla\phi_1}{|P_{\nabla\phi_2}\nabla\phi_1|}\right]\eta\mathrm{d}x \\
&\quad - \varepsilon\int G\delta'(\phi_1)\delta(\phi_2)|\nabla\phi_2||P_{\nabla\phi_2}\nabla\phi_1|\eta\mathrm{d}x. \qquad \text{(B6)}
\end{aligned}$$

The last equality in Eq. (B6) holds due to Eq. (B5), and the second-last equality holds because of the following relation

$$\langle P_{\nabla\phi_2}\nabla\phi_1, \nabla\phi_1\rangle = |P_{\nabla\phi_2}\nabla\phi_1|^2. \qquad \text{(B7)}$$

Now the last term in Eq. (B6) cancels the first term in the *r.h.s.* of Eq. (B2), and we have the first variation

$$\begin{aligned}
&\int G\delta(\phi_1+\varepsilon\eta)\delta(\phi_2)|\nabla\phi_2||P_{\nabla\phi_2}\nabla(\phi_1+\varepsilon\eta)|\mathrm{d}x \\
&= \int G\delta(\phi_1)\delta(\phi_2)|\nabla\phi_2||P_{\nabla\phi_2}\nabla\phi_1|\eta\mathrm{d}x \\
&\quad - \varepsilon\int \delta(\phi_1)\delta(\phi_2)\mathrm{div}\left(G|\nabla\phi_2|\frac{P_{\nabla\phi_2}\nabla\phi_1}{|P_{\nabla\phi_2}\nabla\varphi_1|}\right)\eta\mathrm{d}x + O(\varepsilon^2).
\end{aligned} \qquad \text{(B8)}$$

Thus, the gradient descent direction with respect to ϕ_1 is

$$\delta(\phi_1)\delta(\phi_2)\mathrm{div}\left(G|\nabla\phi_2|\frac{P_{\nabla\phi_2}\nabla\phi_1}{|P_{\nabla\phi_2}\nabla\phi_1|}\right). \qquad \text{(B9)}$$

The gradient descent direction for ϕ_2 can be similarly derived.

Appendix C

In order to calculate the Euler–Lagrange equation of the second matching term $\sum_j T_P\left(Q^j|_{g^{-1}(x,1)}\right)$ whose integral form involves the map $g(x,t)$, we need the corresponding perturbation of the mapping g under a perturbation of v: $v \to v + \varepsilon\eta$. As shown in Miller et al. (2002), the perturbation in g is

$$g \to g + \varepsilon Dg(x,1)\int_0^1 \left(Dg(x,t)\right)^{-1}\eta(g(x,t),t)\mathrm{d}t. \qquad \text{(C1)}$$

Using the above result, we now calculate the variation of the second matching term under the perturbation of v. For simplicity, we will use the dual of the least-square cost function: $||S(x)-T(g(x,1))||^2$ for our derivation. The first variation in this case amounts to the following

$$\begin{aligned}
&\int_\Omega (S(x) - T(g(x,1)))\nabla T(g(x,1)) \\
&\quad\times\left\{D(g(x,1))\int_0^1 D(g(x,t))^{-1}\eta(g(x,t),t)\mathrm{d}t\right\}\mathrm{d}x \\
&\quad = \int_\Omega\int_0^1 (S(x) - T(g(x,1)))\nabla T(g(x,1))D(g(x,1)) \\
&\qquad\times D(g(x,t))^{-1}\eta(g(x,t),t)\mathrm{d}t\mathrm{d}x.
\end{aligned} \qquad \text{(C2)}$$

Using change of variable $\xi = g(x,t)$, we obtain

$$\begin{aligned}
&\int_\Omega\int_0^1 (S(x) - T(g(x,1)))\nabla T(g(x,1))D(g(x,1)) \\
&\quad\times D(g(x,t))^{-1}\eta(g(x,t),t)\mathrm{d}t\mathrm{d}x \\
&\quad = \int_\Omega\int_0^1 \left(S\left(g^{-1}(\xi,t)\right) - T\left(g_1g_t^{-1}(\xi)\right)\right) \\
&\qquad\times \nabla T\left(g_1g_t^{-1}(\xi)\right)D\left(g_1g_t^{-1}(\xi)\right)\eta\left(\xi,t\right)|Dg^{-1}(\xi,t)|\mathrm{d}t\mathrm{d}\xi.
\end{aligned} \qquad \text{(C3)}$$

Thus, for $\forall x\in\Omega$, the first variation of the cost functional $||S(x)-T(g(x,1))||^2$ at time t has the following terms

$$\begin{aligned}
&\left(S\left(g^{-1}(x,t)\right) - T\left(g_1g_t^{-1}(x)\right)\right)\nabla T\left(g_1g_t^{-1}(x)\right) \\
&\quad\times D\left(g_1g_t^{-1}(x)\right)|Dg^{-1}(x,t)|.
\end{aligned} \qquad \text{(C4)}$$

Notice again the duality between Eq. (C4) and the gradient descent in Eq. (18) for the least-square cost functional.

Following similar calculations, we obtain the body force contributed by the matching term $\sum_j T_P\left(Q^j|_{g^{-1}(x,1)}\right)$ using the notation Eq. (6)

$$\begin{aligned}
&-\sum_j\left\{\prod_n \delta\left(\psi_n^j\circ g_1g_t^{-1}\right)\sum_n f_n\left(T_P\circ g^{-1}(x,t)\Psi^j\circ g_1g_t^{-1}\right)\nabla\left(\psi_n^j\circ g_1g_t^{-1}\right)\right\} \\
&\quad\times|Dg^{-1}(x,t)|.
\end{aligned} \qquad \text{(C5)}$$

References

Ashburner, J., Hutton, C., Frackowiak, R., Johnsrude, I., Price, C., Friston, K., 1998. Identifying global anatomical differences: deformation-based morphometry. Hum. Brain Mapp. 6, 348–357.

Avants, B., Gee, J., 2004. Geodesic estimation for large deformation anatomical shape averaging and interpolation. In: Thompson, P.M.,

Miller, M.I., Ratnanather, J.T., Poldrack, R., Nichols, T.E. (Eds.), Special Issue on Mathematics in Brain Imaging, NeuroImage. September.

Bajcsy, R., Kovacic, S., 1989. Multiresolution elastic matching. Comput. Vis. Graph. Image Process. 46, 1–21.

Bertalmío, M., Sapiro, G., Randall, G., 1999. Region tracking on level-sets methods. IEEE Trans. Med. Imag. 18 (5), 448–451.

Bookstein, F.L., 1978. Lecture Notes in Biomathematics. vol. 24. Springer-Verlang, New York.

Bro-Nielsen, M., Gramkow, C., . Fast fluid registration of medical images. Proc. Visualization in Biomedical Computing (VBC'96), Hamburg, Germany, Springer Lect. Notes Comput. Sci., vol. 1131. pp. 267–276.

Burchard, P., Cheng, L.T., Merriman, B., Osher, S., 2001. Motion of curves in three spatial dimensions using a level set approach. J. Comput. Phys. 170 (2), 720–741.

Cheng, L.T., Burchard, P., Merriman, B., Osher, S., 2002. Motion of curves constrained on surfaces using a level-set approach. J. Comput. Phys. 175 (2), 604–644.

Christensen, G.E., Johnson, H.J., 2001. Consistent image registration. IEEE Trans. Image Process. 20, 568–582.

Christensen, G.E., Rabbitt, R.D., Miller, M.I., 1996. Deformable templates using large deformation kinematics. IEEE Trans. Image Process. 5, 1435–1447.

Christensen, G.E., Joshi, S.C., Miller, M.I., 1997. Volumetric transformation of brain anatomy. IEEE Trans. Med. Imag. 16, 864–877.

Chung, M.K., Worsley, K.J., Paus, T., Cherif, C., Giedd, J.N., Rapoport, J.L, Evans, A.C., 2001. A unified statistical approach to deformation-based morphometry. NeuroImage 14, 595–606.

Chung, M.K., Dalton, K.M., Alexander, A.L., Davidson, R.J., 2004. Less white matter concentration in autism: 2D voxel-based morphometry. NeuroImage (in press).

Collins, D.L., Holmes, C.J., Peters, T.M., Evans, A.C., 1995. Automatic 3D model-based neuroanatomical segmentation. Hum. Brain Mapp. 3, 190–208.

Davatzikos, C., Resnick, S.M., 1998. Sex differences in anatomic measures of interhemispheric connectivity: correlations with cognition in women but not men. Cereb. Cortex 8, 635–640.

Davatzikos, C., Vaillant, M., Resnick, S., Prince, J.L., Letovsky, S., Bryan, R.N., 1996a. A computerized method for mopological analysis of the corpus callosum. J. Comput. Assist. Tomogr. 20, 88–97.

Davatzikos, C.A., Prince, J.L., Bryan, R.N., 1996b. Image registration based on boundary mapping. IEEE Trans. Med. Imag. 15, 112–115.

Dupuis, P., Grenander, U., Miller, M.I., 1998. Variational problems on flows of diffeomorphisms for image matching. Q. Appl. Math. 56, 587–600.

Fischl, B., Sereno, M.I., Tootell, R.B.H., Dale, A.M., 1999. High-resolution inter-subject averaging and a coordinate system for the cortical surface. Hum. Brain Mapp. 8, 272–284.

Fischl, B., Liu, A., Dale, A.M., 2001. Automated manifold surgery: constructing geometrically accurate and topologically correct models of the human cerebral cortex. IEEE Trans. Med. Imag. 20, 70–80.

Gogtay, N., Giedd, J.N., Lusk, L., Hayashi, K.M., Greenstein, D., Vaitiuzis, C., Nugent, T.F., Herman, D.H., Classen, L., Toga, A.W., Rapoport, J.L., Thompson, P.M., 2004. Dynamic mapping of human cortical development during childhood and adolescence. Proc. Natl. Acad. Sci. 101, 8174–8179.

Grenander, U., Miller, M.I., 1998. Computational anatomy: an emerging discipline. Q. Appl. Math. 56, 617–694.

Holm, D., Ratnanather, T., Trouvé, A., Younes, L., 2004. Soliton dynamics in computational anatomy. In: Thompson, P.M., Miller, M.I., Ratnanather, J.T., Poldrack, R., Nichols, T.E. (Eds.), Special Issue on Mathematics in Brain Imaging, NeuroImage. September.

Hurdal, M.K., Stephenson, K., 2004. Cortical cartography using the discrete conformal approach of circle packings. In: Thompson, P.M., Miller, M.I., Ratnanather, J.T., Poldrack, R., Nichols, T.E. (Eds.), Special Issue on Mathematics in Brain Imaging, NeuroImage. September.

Janke, A.L., de Zubicaray, G., Rose, S.E., Griffin, M., Chalk, J.B., Galloway, G.J., 2001. 4D deformation modeling of cortical disease progression in Alzheimer's dementia. Magn. Reson. Med. 46, 661–666.

Joshi, S.C., Miller, M.I., 2000. Landmark matching via large deformation diffeomorphisms. IEEE Trans. Image Process. 9, 1357–1370.

Joshi, S.C., Miller, M.I., Christensen, G.E., Banerjee, A., Coogan, T.A., Grenander, U., 1995. Hierarchical brain mapping via a generalized dirichlet solution for mapping brain manifolds, vision geometry IV. Conference on Optical Science, Engineering and Instrumentation, San Diego, California. pp. 278–289.

Lancaster, J.L., Kochunov, P.V., Thompson, P.M., Toga, A.W., Fox, P.T., 2003. Asymmetry of the brain surface from deformation field analysis. Hum. Brain Mapp. 19, 79–89.

Leow, A., Chiang, M.C., Protas, H., Thompson, P., Vese, L.A, Huang, S.C., 2004a. Linear and non-linear geometric object matching with implicit representations. Presented at ICPR, Cambridge, United Kingdom.

Leow, A., Thompson, P., Protas, H., Huang, S.C., 2004b. Brain warping with implicit representations. Presented at ISBI, Arlington, Virginia.

Liao, W.H. 2003. Mathematical techniques in object matching and computational anatomy: a new framework based on the level set method. PhD dissertation in Department of Biomathematics. UCLA.

Liao, W.H., Vese, L., Huang, S.C., Bergsneider, M., Osher, S., 2003. Computational anatomy and implicit object representation: a level set approach. Lect. Notes Comput. Sci., 40–49.

Mazziotta, J.C., Toga, A.W., Evans, A.C., Fox, P.T., Lancaster, J., Zilles, K., Woods, R.P., Paus, T., Simpson, G., Pike, B., Holmes, C.J., Collins, D.L., Thompson, P.M., MacDonald, D., Schormann, T., Amunts, K., Palomero-Gallagher, N., Parsons, L., Narr, K.L., Kabani, N., Le Goualher, G., Boomsma, D., Cannon, T., Kawashima, R., Mazoyer, B., 2001. A probabilistic atlas and reference system for the human brain [Invited Paper]. J. R. Soc. 356, 1293–1322.

Miller, M.I., 2004. The emerging field of computational anatomy. In: Thompson, P.M., Miller, M.I., Ratnanather, J.T., Poldrack, R., Nichols, T.E. (Eds.), Special Issue on Mathematics in Brain Imaging, NeuroImage. September.

Miller, M.I., Trouve, A., Younes, L., 2002. On the metrics and Euler–Lagrange equations of computational anatomy. Annu. Rev. Biomed. Eng. 4, 375–405.

Narr, K.L., Thompson, P.M., Sharma, T., Moussai, J., Cannestra, A.F., Toga, A.W., 2000. Mapping corpus callosum morphology in schizophrenia. Cereb. Cortex 10, 40–49.

Narr, K.L., Cannon, T.D., Woods, R.P., Thompson, P.M., Kim, S., Asunction, D., van Erp, T.G., Poutanen, V.P., Huttunen, M., Lonnqvist, J., Standerksjold-Nordenstam, C.G., Kaprio, J., Mazziotta, J.C., Toga, A.W., 2002. Genetic contributions to altered callosal morphology in schizophrenia. J. Neurosci. 22, 3720–3729.

Nielsen, M., Florack, L., Deriche, R., 1994. Regularization and scale space: INRIA Technical Report.

Osher, S., Sethian, J., 1988. Fronts propagating with curvature-dependent speed: algorithms based on Hamilton–Jacobi formulations. J. Comput. Phys. 79, 1–49.

Pennec, X., Fillard, P., Ayache, N., 2004. A riemannian framework for tensor computing. Research Report 5255, INRIA, July 2004.

Pettey, D.J., Gee, J.C., 2001. Using a linear diagnostic function and non-rigid registration to search for morphological differences between populations: an example involving the male and female corpus callosum. IPMI, 372–379.

Rey, D., Subsol, G., Delingette, H., Ayache, N., 1999. Using continuum mechanics operators for detection and quantification of evolving processes in 3D medical images. EUROMECH'99, Warsaw, Poland. pp. 185–188. May.

Rohr, K., Stiehl, H.S., Sprengel, R., Beil, W., Buzug, T.M., Weese, J., Kuhn, M.H., 1996. Point-based elastic registration of medical image data using approximating thin-plate splines. In: Höhne, K.H., Kikinis, R. (Eds.), Visualization in Biomedical Computing, Lecture Notes in Computer Science. vol. 1131. Springer, Hamburg, Germany, pp. 297–306.

Sereno, M.I., Dale, A.M., Liu, A., Tootell, R.B., 1996. A surface-based coordinate system for a canonical cortex. 2nd International Conference Human Brain Mapping, Boston, Massachusetts NeuroImage. vol. S252.

Shen, D., Davatzikos, C., 2003. Very high resolution morphometry using mass-preserving deformations and HAMMER elastic registration. NeuroImage 18, 28–41.

Sowell, E.R., Mattson, S.N., Thompson, P.M., Jernigan, T.L., Riley, E.P., Toga, A.W., 2001. Mapping callosal morphology and cognitive correlates: effects of heavy prenatal alcohol exposure. Neurology 57, 235–244.

Studholme, C., Cardenas, V., Blumenfeld, R., Schuff, N., Rosen, H.J., Miller, B., Weiner, M., 2004. Deformation tensor morphometry of semantic dementia with quantitative validation. NeuroImage 21, 1387–1398.

Subsol, G., 1999. Crest lines for curve-based warping. In: Toga, A. (Ed.), Brain Warping. Academic Press, San Diego, pp. 241–262.

Thirion, J.-P., Prima, S., Subsol, S., 2000. Statistical analysis of dissymmetry in volumetric medical images. Med. Image Anal. 4, 111–121.

Thompson, P.M., Toga, A.W., 1996. A surface-based technique for warping three-dimensional images of the brain. IEEE Trans. Med. Imag. 15, 1–16.

Thompson, P.M., Toga, A.W., 1997. Detection, visualization and animation of abnormal anatomic structure with a deformable probabilistic brain atlas based on random vector field transformations. Med. Image Anal. 1, 271–294.

Thompson, P., Toga, A.W., 2002. A framework for computational anatomy. Comput. Vis. Sci. 5, 13–34.

Thompson, P.M., MacDonald, D., Mega, M.S., Holmes, C.J., Evans, A.C., Toga, A.W., 1997. Detection and mapping of abnormal brain structure with a probabilistic atlas of cortical surfaces. J. Comput. Assist. Tomogr. 21, 567–581.

Thompson, P.M., Giedd, J.N., Woods, R.P., MacDonald, D., Evans, A.C., Toga, A.W., 2000a. Growth patterns in the developing brain detected by using continuum-mechanical tensor maps. Nature 404, 190–193.

Thompson, P.M., Woods, R.P., Mega, M.S., Toga, A.W., 2000b. Mathematical/computational challenges in creating population-based brain atlases [Invited Paper]. Hum. Brain Mapp. 9, 81–92.

Thompson, P.M., Hayashi, K.M., de Zubicaray, G., Janke, A.L., Rose, S.E., Semple, J., Herman, D., Hong, M.S., Dittmer, S., Doddrell, D.M., Toga, A.W., 2003a. Dynamics of gray matter loss in Alzheimer's disease. J. Neurosci. 23, 994–1005.

Thompson, P.M., Narr, K.L., Blanton, R.E., Toga, A.W., 2003b. Mapping structural alterations of the corpus callosum during brain development and degeneration. In: Zaidel, E., Iacoboni, M. (Eds.), The Parallel Brain: the Cognitive Neuroscience of the Corpus Callosum. MIT Press.

Thompson, P.M., Hayashi, K.M., Sowell, E.R., Gogtay, N., Giedd, J.N., Rapoport, J.L., de Zubicaray, G.I., Janke, A.L., Rose, S.E., Semple, J., Doddrell, D.M., Wang, Y.L., van Erp, T.G.M., Cannon, T.D., Toga, A.W., 2004. Mapping cortical change in Alzheimer's disease, brain development, and schizophrenia. In: Thompson, P.M., Miller, M.I., Ratnanather, J.T., Poldrack, R., Nichols, T.E. (Eds.), Special Issue on Mathematics in Brain Imaging, NeuroImage. September.

Trouve, A., 1998. Diffeomorphisms groups and pattern matching in image analysis. Int. J. Comput. Vis. 28, 213–221.

Tikhonov, A.N., Arsenin, V.Y., 1977. Solutions of Ill Posed Problems. W.H. Winston, Washington, DC.

Toga, A.W., 1998. Brain Warping. Academic Press, New York.

Vaillant, M., Miller, M.I., Younes, L., Trouve, A., 2004. Linear statistics for diffeomorphic shape evolution via geodesic shooting. In: Thompson, P.M., Miller, M.I., Ratnanather, J.T., Poldrack, R., Nichols, T.E. (Eds.), Special Issue on Mathematics in Brain Imaging, NeuroImage. September.

van Essen, D.C., 2004. Surface-based approaches to spatial localization and registration in primate cerebral cortex. In: Thompson, P.M., Miller, M.I., Ratnanather, J.T., Poldrack, R., Nichols, T.E. (Eds.), Special Issue on Mathematics in Brain Imaging, NeuroImage. September.

Vidal, C.N., DeVito, T.J., Hayashi, K.M., Drost, D.J., Williamson, P.C., Craven-Thuss, B., Herman, D., Sui, Y., Toga, A.W., Nicolson, R., Thompson, P.M., 2003. Detection and visualization of corpus callosum deficits in autistic children using novel anatomical mapping algorithms. Proceedings of International Society for Magnetic Resonance in Medicine (ISMRM) 2003, Toronto, Canada.

Woods, R.P., 2003. Characterizing volume and surface deformations in an atlas framework: theory, applications, and implementation. NeuroImage 18, 769–788.

Woods, R.P., Mazziotta, J.C., Cherry, S.R., 1993. MRI-PET registration with automated algorithm. J. Comput. Assist. Tomogr. 17, 536–546.

Woods, R.P., Grafton, S.T., Watson, J.D., Sicotte, N.L., Mazziotta, J.C., 1998. Automated image registration: II. Intersubject validation of linear and nonlinear models. J. Comput. Assist. Tomogr. 22, 153–165.

Zeineh, M.M., Engel, S.A., Thompson, P.M., Bookheimer, S., 2003. Dynamics of the hippocampus during encoding and retrieval of face-name pairs. Science 299, 577–580.